minerals

MDPI

Article

The Influence of Fluid-Exsolving Depth on Mineralization Quality: Evidence from Biotite and Zircon Mineralogy and Fluid Inclusions from the 460 Gaodi Porphyry Mo-Cu Deposit, NE China

Jing Kan [1,2], Kezhang Qin [1,2,*], Le Wang [1,3], Kaixuan Hui [1,2] and Ri Han [1,2]

[1] Key Laboratory of Mineral Resources, Institute of Geology and Geophysics, Chinese Academy of Sciences, Beijing 100029, China; 15046281908@163.com (J.K.)
[2] College of Earth and Planetary Sciences, University of Chinese Academy of Sciences, Beijing 101408, China
[3] Department of Earth Sciences, University of Geneva, 1205 Geneva, Switzerland
* Correspondence: kzq@mail.iggcas.ac.cn

Abstract: The recently discovered 460 Gaodi porphyry Mo-Cu deposit is a sub-economic deposit characterized by low Mo-Cu grades, dispersed mineralization, and separated Mo- and Cu-ore bodies. This study aims to elucidate the factors underlying this type of sub-economic mineralization. Electron-microprobe analyses of biotite from ore-related granite porphyry yielded Ti-in-biotite crystallization temperatures of 677–734 °C (an average of 719 °C) and biotite phenocryst crystallization depths of 6.0 to 12.9 km. LA-ICP-MS analyses of zircons from the same sample revealed average zircon Ce^{4+}/Ce^{3+} ratios of 299.7 and elevated zircon lg(fO_2) ratios, with an average ΔFMQ of +6.6 ± 1.9. These discoveries suggest that the magma responsible for ore formation boasts a high degree of oxidation, yet also possesses a magma chamber located at a significant depth within the upper crust. This implies an extensive exsolving depth for fluids. Furthermore, our microthermometry analysis of fluid inclusions reveals that a portion of the fluid experiences considerable conductive cooling as it ascends along the conduit, owing to the depth of fluid exsolution. This process results in the ore fluids remaining in the liquid-only region without undergoing boiling, which is conducive to the enrichment of metals. We emphasize the fact that fluid-exsolving depth plays a critical role in determining the metal grades and economic value of a porphyry deposit by regulating the P-T evolution path of the ore fluids

Keywords: 460 Gaodi porphyry Mo-Cu deposit; biotite-zircon mineralogy; fluid-exsolving depth; oxygen fugacity; fluid inclusion

Citation: Kan, J.; Qin, K.; Wang, L.; Hui, K.; Han, R. The Influence of Fluid-Exsolving Depth on Mineralization Quality: Evidence from Biotite and Zircon Mineralogy and Fluid Inclusions from the 460 Gaodi Porphyry Mo-Cu Deposit, NE China. *Minerals* **2023**, *13*, 699. https://doi.org/10.3390/min13050699

Academic Editor: David Lentz

Received: 18 April 2023
Revised: 16 May 2023
Accepted: 17 May 2023
Published: 20 May 2023

1. Introduction

Northeast China (Figure 1a) is the largest Mo metallogenic province in the world [1,2] and also an important Cu metallogenic province in China [3]. In particular, in the northern Great Xing'an Range (GXR), several porphyry Cu-Mo deposits have been identified, including Duobaoshan Cu-Mo-(Au) [4], Tongshan Cu-Mo [5], Wunugetushan Cu-Mo [6,7], Xiaokelehe Cu-Mo [8], Fukeshan Cu-Mo [9], Yili Mo [10], and numerous ore occurrences. While other factors must be taken into account, an examination of the geology of these deposits reveals that some have not yet been mined, due to a discrepancy between their mineralization quality and the requirements for industrial mining. The intrinsic value of mineralization quality is determined by its industrial value and mining difficulty. An economic deposit is characterized by large scale, high grade, concentrated ore bodies, favorable ore body shape (tubular, thick plate, giant lenticular), and shallow burial. In contrast, a sub-economic deposit exhibits low grade, scattered multiple orebodies, poor ore body shape (veined, annular, lenticular, multi-layered), and deep burial. Understanding

the factors that govern deposit quality is crucial for identifying fertile porphyry systems and guiding exploration efforts.

Previous research has demonstrated that the formation of a high-quality porphyry Cu-Au deposit necessitates the presence of sufficient volumes of fertile magma in conjunction with efficient hydrothermal transport mechanisms and ore depositional processes [11,12]. Failure of any of these steps early in the process can diminish the potential for economic ore formation and result in belt-scale barren systems [13]. Several factors may influence mineralization quality, including magma water content [14], magmatic oxygen fugacity (fO_2) [15,16], fluid focusing induced by structural systems [17–20], and phase transition paths of ore-forming fluids [21–23]. However, fluid-exsolving depth (pressure) as a single variable may affect the initial compositions of the porphyry system [24–28], the structural system governing the transport and precipitation of ore-forming materials [29,30], and phase transition paths of ore-forming fluids [21,31–34]. Concurrently, several studies have confirmed its significant role in determining the mineralization form of the deposit [14,35–38].

The 460 Gaodi porphyry Mo-Cu deposit (Gaodi: highland), situated 30 km west of Hanjiayuanzi town in northern GXR, was newly discovered in 2019 by the No.9 Geological Exploration Institute of Heilongjiang Province and is currently undergoing exploration. Preliminary estimates by the authors indicate total metal reserves of 50 kt @0.066% Mo and 100 kt @0.42% Cu, with a mineralization age of 179.6 ± 3.6 Ma (molybdenite Re-Os age in another to-be-published study). This deposit is characterized by a relatively deep burial depth, low metal grade, dispersed mineralization, and separated Mo and Cu ore bodies. Although classified as a sub-economic deposit in terms of mining, it presents a valuable opportunity to investigate the factors governing this type of mineralization.

The analysis of fluid inclusions can yield insights into fluid phase transformation processes. The chemical composition of primary magmatic biotite [39] closely reflects the igneous petrology, petrogenesis, crystallization depth, and fO_2 of the host magmas [40,41]. Additionally, zircon offers a unique means of obtaining absolute fO_2 values for a magmatic suite [42,43]. In this study, we employed new biotite composition data to investigate the petrogenetic origin, temperature, and crystallization depth (pressure) of biotite from the ore-forming porphyry. The redox state was quantitatively calculated using zircon trace elements. We also analyzed a pre-ore monzogranite sample that spatially coexisted with the ore-forming porphyry, for comparative purposes. Finally, fluid evolution during the hydrothermal stage was traced using fluid inclusion microthermometry and the impact of fluid-exsolving depth on mineralization quality was further discussed.

2. Geological Setting

2.1. Regional Geology

The tectonic position of the study area is located in the northeast of the GXR (Figure 1a,b), near the Xinlin–Xiguitu suture, which is the junction of the Ergun block and the Xing'an block [44].

The regional strata consist of the Meso–Neoproterozoic Xinghuadukou Group (Pt_3xh) metamorphic rocks, the Upper Jurassic Manitu Formation (J_3mn) trachyte andesite and andesitic tuffs, the Lower Cretaceous Guanghua Formation (K_1gn) tuffs and the Quaternary sediments (Qh). The intrusive rocks are mainly composed of Early Ordovician granodiorite, Late Carboniferous granite ($C_3\gamma$), monzogranite ($C_3\eta\gamma$), granodiorite ($C_3\gamma\delta$), Late Triassic–Early Jurassic granite ($T_3J_1\gamma$), monzogranite ($T_3J_1\eta\gamma$), and Late Jurassic–Early Cretaceous quartz syenogranite ($J_3K_1\xi o$), distributed as stocks and dikes of different sizes. There is a volcanic ring tectonic uplift developed in the west of this area (Figure 1c), with a related annular fracture F3, named the Shitoushan Fault. With a length of 20 km, F3 is closely related to mineralization, as its wall rocks are Mesozoic intrusions and the Manitu and Guanghua Formation erupted along the circular fault fissures. F4 and F9 are both post-mineralization fractures.

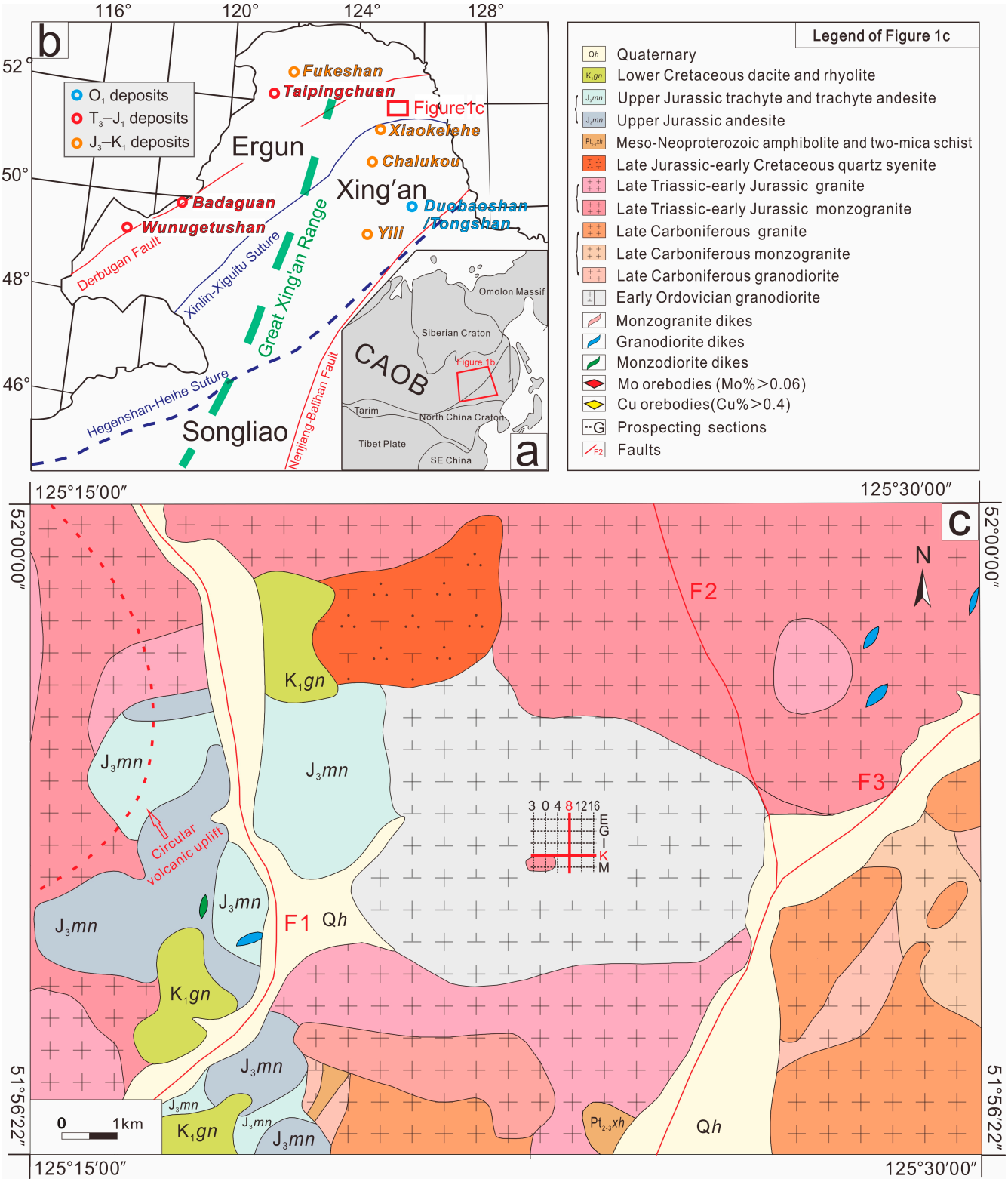

Figure 1. Tectonic location and geological maps of the 460 Gaodi deposit. (**a**) Sketch map of the eastern section of Central Asian Orogenic Belt (CAOB), modified after [45]; (**b**) map of the structural framework of the northern Great Xing'an Range and porphyry Cu–Mo deposits' locations, modified after [46]; (**c**) regional geological map of the 460 Gaodi deposit, after geological data from No.9 Geological Exploration Institute of Heilongjiang Province.

2.2. Geology of the 460 Gaodi Deposit

2.2.1. Strata, Structure and Magmatic Rocks

Except for a small amount of Quaternary Holocene (Qh) flood plain accumulation and widely distributed weathering layer coverage, there are no other exposed strata in the ore district (Figure 2a,b). Together with regional structural characteristics and geophysical, geochemical and geological data, seven faults, mainly in NEE and near NW, are inferred (Figure 2a). Some faults control the occurrence of fracture zones and dikes, but do not cut orebodies. Intrusive rocks are widely developed around the study area and covered by sediments. Abrupt contact relations between some of them can be observed in the drill holes. According to the dating results (our unpublished data), the intrusions can be divided into four stages: Early Ordovician, Late Triassic, early Early Jurassic and late Early Jurassic. Among them, Early Ordovician granodiorite has the largest surface area of ~12 km^2, a length of ~7.2 km, and a width of ~4.5 km, with a NW dip at ~80°. It occurs as batholith and is intruded by other late-stage, small-scale dikes (Figure 2b).

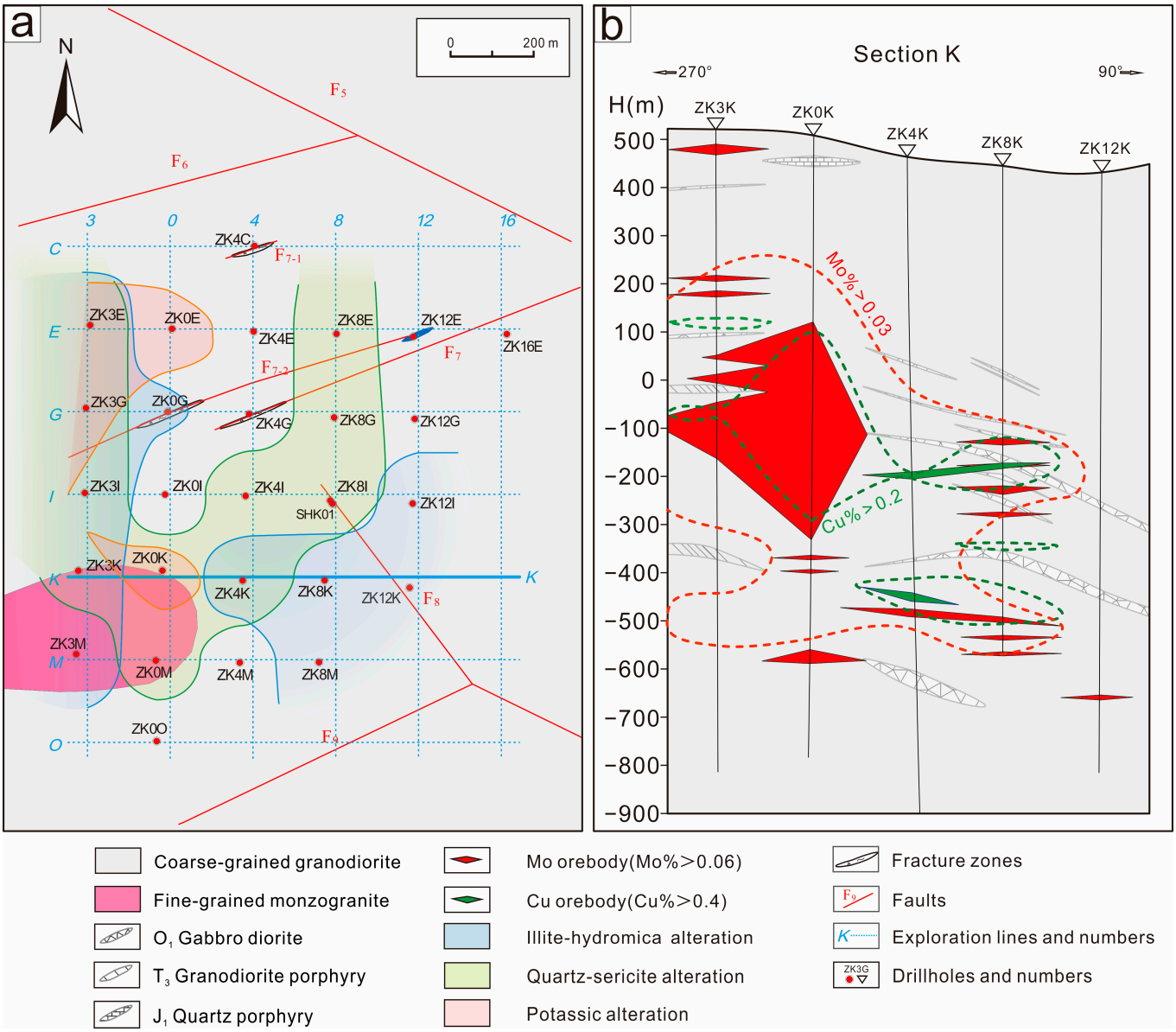

Figure 2. (**a**) Geological map of the mining area, and (**b**) geological section of Line K.

2.2.2. Wall Rock Alteration, Mineralization and Mineralization Stage

The 460 Gaodi Mo-Cu deposit primarily consists of porphyry Mo mineralization with subordinate Cu and minor Pb-Zn mineralization. The deposit contains two types of orebodies, the first type being irregular columnar Mo ore bodies centered around drill hole 0 K (Figure 2b), approximately 600 m in length, 400 m in width, and 400 m in height, which mainly contain molybdenite and minor chalcopyrite (Figure 3a–d), occurring in complex interlaced quartz veinlets with a width averaging 2–4 mm and up to 15 cm (Figure 3a,b), as well as disseminated veinlets (Figure 3d). No independent economic Cu ore body was discovered within these Mo ore bodies. The second mineralization type occurs in small-dip layered and banded Mo and Cu ore bodies occurring at depth, as well as at the top and edge of the main ore body (Figure 2b). There are about 30 such ore bodies, each with lengths ranging from 50 to 250 m, widths ranging from 50 to 200 m, and a general thickness ranging from 8 to12 m at inclinations between 0 and 15 degrees. The Mo and Cu orebodies are separate. The Mo orebodies mostly consist of molybdenite-quartz ± calcite ± sericite veinlets (Figure 3a–f) or disseminated veinlets with minor chalcopyrite (Figure 3g). The Cu ore bodies are mostly comprised of coarse chalcopyrite-quartz ± molybdenite veinlets or chalcopyrite-pyrite-quartz-chlorite veins (Figure 3h). In addition, some quartz-sphalerite-galena ± chalcopyrite veins develop in distal parts (Figure 3i).

Hydrothermal alteration affected the 460 Gaodi deposit widely, producing a zoned pattern (Figure 4) of potassic (biotite (Figure 3) and K-feldspar (Figure 3k)), phyllic (Figure 3a,e,f), illite–hydromuscovite (Figure 3l) (hydromuscovite and kaolinite), and propylitic (chlorite (Figure 3h) and carbonate) alteration zones from the bottom to the top zone. Potassic zones are usually vertically overprinted by phyllic zones, which exhibit vague zonations (Figure 4). Potassic zones are generally associated with minor Mo mineralization, while phyllic zones are associated with Mo and minor Cu mineralization, and propylitic zones are associated with Cu-Pb-Zn mineralization.

Five paragenetic stages have been identified on the basis of crosscutting relationships, mineral assemblages, and related alteration of hydrothermal veins: stage 1 premineralization, stage 2 Mo mineralization, stage 3 pyrite-sericite, stage 4 Cu-Mo mineralization, and stage 5 late-mineralization.

The premineralization stage (stage 1) is characterized by sulfide-barren quartz veins, K-feldspar-quartz ± calcite ± sericite veins, and hydrothermal biotite veins that predominantly developed in the lower portion of the deposit and exhibit variable irregular-to-straight textures. These veins are associated with potassic alteration and are manifested as K-feldspar-dominant alteration halos, with minor biotite alteration halos. The Mo mineralization stage (stage 2) is distinguished by quartz-molybdenite ± K-feldspar ± calcite veins and is most prevalent in the main ore body, which assumes a columnar shape centered around borehole 0K. The pyrite-sericite stage (stage 3) represents a transitional stage characterized by barren pyrite-sericite ± quartz and sulfide-barren quartz veins that primarily occur within the quartz-sericite zones. As a subordinate mineralization stage, the Cu-Mo mineralization stage (stage 4) is dominated by veins comprising complex mineral assemblages consisting primarily of molybdenite, chalcopyrite, and quartz, with subordinate sericite, pyrite, bornite, tetrahedrite, galena, sphalerite, calcite, etc. These veins form the aforementioned banded Mo and Cu subordinate ore bodies. Although the Cu and Mo ore bodies are separated, this is primarily reflected in the content of chalcopyrite and molybdenite within the veins comprising the ore body, with little difference in their mineral assemblages. The late-mineralization stage (stage 5) is characterized by quartz-pyrite-chlorite-calcite ± epidote ± sericite ± chalcopyrite ± galena ± sphalerite veins that are predominantly distributed at the periphery of the deposit.

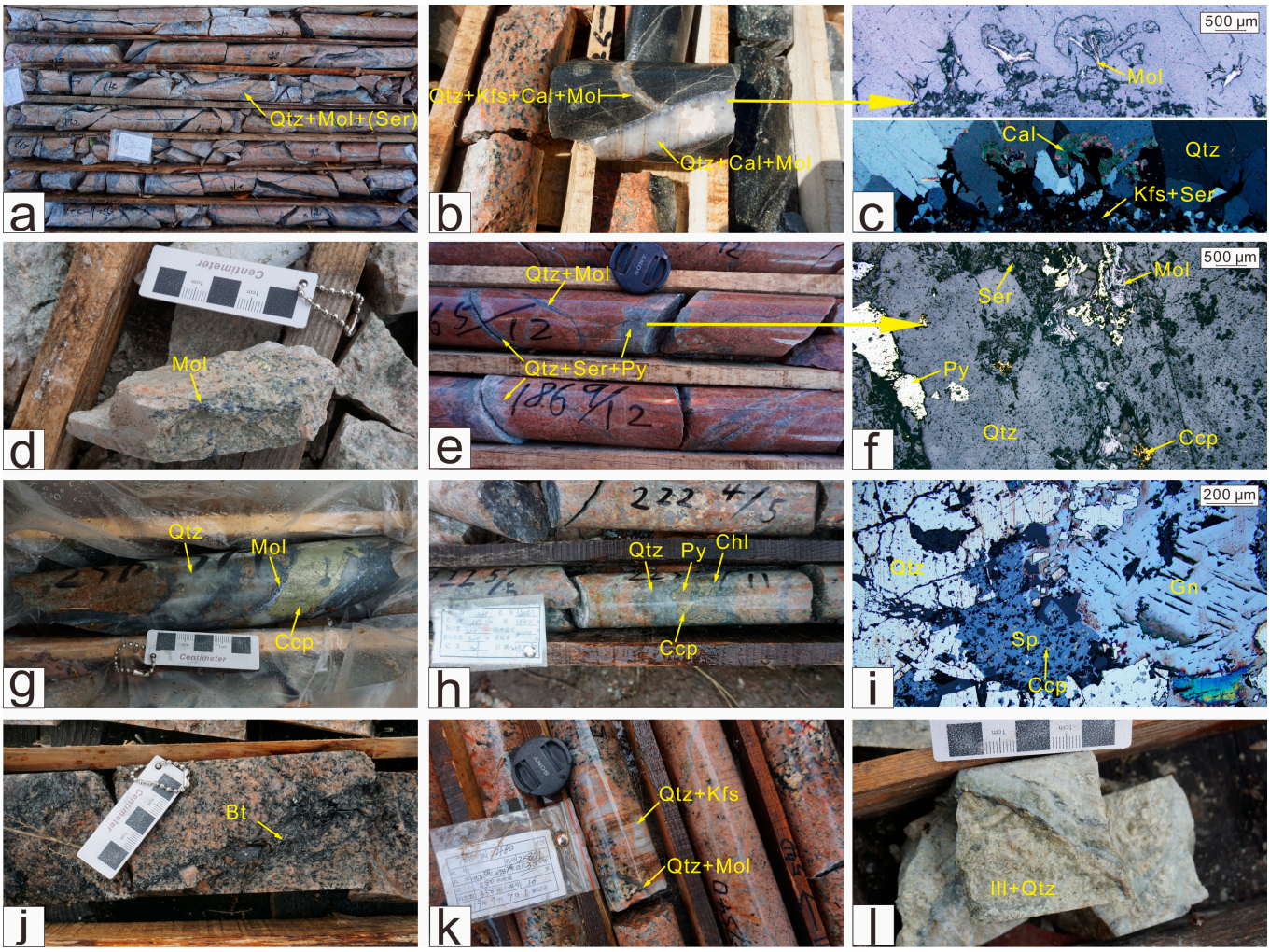

Figure 3. Photographs and photomicrographs of alteration and mineralization in the 460 Gaodi deposit. (**a**) Complex interlaced quartz–molybdenite–(sericite) veinlets in the main Mo orebody; (**b**) quartz calcite–K-feldspar–molybdenite veinlet cut by quartz–molybdenite–calcite vein; (**c**) quartz–K-feldspar–calcite–sericite–molybdenite coexist, with reflected light on the top and crossed polarized light on the bottom; (**d**) disseminated Mo veinlets; (**e**) quartz–sericite–pyrite veins cut by quartz–molybdenite veinlets; (**f**) quartz–sericite–chalcopyrite–molybdenite coexist in the quartz–sericitization zone; (**g**) quartz–chalcopyrite–molybdenite coexist in the banded Cu orebodies; (**h**) quartz–chlorite–pyrite–chalcopyrite vein; (**i**) Pb–Zn mineralization in propylitization zone; (**j**) biotization in potassic zone; (**k**) quartz–K-feldspar vein cut by quartz–molybdenite–veinlets; (**l**) illitized and silicified granite. Abbreviations: Qtz = quartz; Kfs = K-feldspar; Ser = sericite; Bt = biotite; Cal = calcite; Chl = chlorite; Ill = illite; Ccp = chalcopyrite; Mol = molybdenite; Sp = sphalerite; Gn = galena; Py = pyrite.

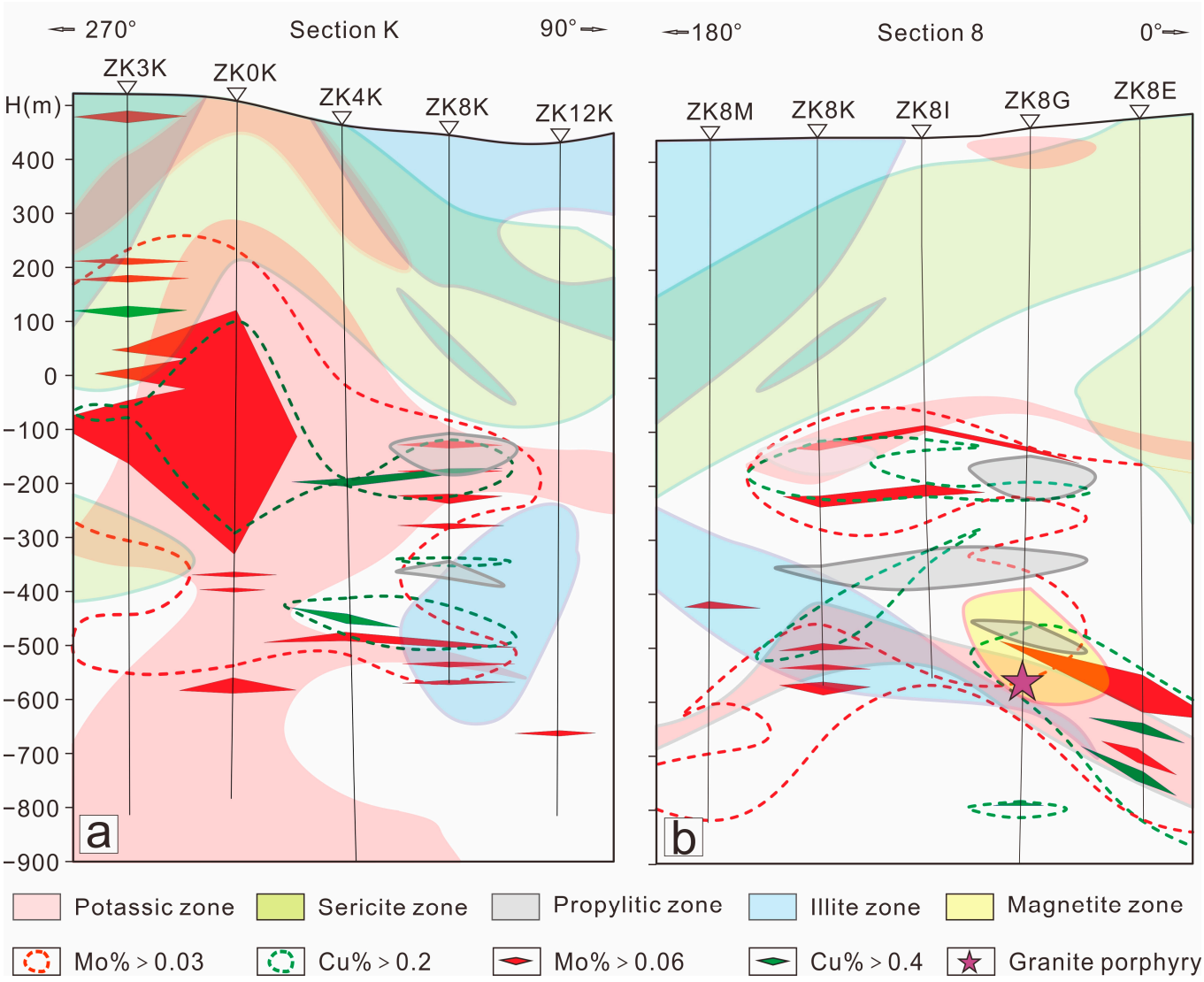

Figure 4. Sectional drawing of (**a**) Line K and (**b**) Line 8 showing alteration zoning and mineralization zoning.

3. Samples and Analytical Methods

3.1. Samples and Petrography

Pre-ore monzogranite (Figure 5a) and ore-related granite porphyry (Figure 5b) with similar crystallization ages were selected from 460 Gaodi for further analyses.

3.1.1. Pre-Ore Monzogranite

The monzogranite intruded into the Early Ordovician granodiorite in multiple vein-like forms. It is mottled in color and consists of 35 vol% K-feldspar, 35 vol% quartz, 20 vol% plagioclase (An_{24} oligoclase), 10 vol% biotite, and minor amphibole (Figure 5c). It crystallized at 198 ± 1 Ma (zircon U-Pb age, from our unpublished data), formed before mineralization.

3.1.2. Ore-Related Granite Porphyry

The Early Jurassic granite porphyry studied occurs as dikes intruding into the Early Ordovician granodiorite in the deep part of drill hole 8G (with a boring-core of ~10 m) (Figure 4b). The phenocryst (35%) consists of K-feldspar (35–45 vol%), plagioclase (10 vol%, two types, An_{23} oligoclase and An_{36} andesine), quartz (45–50 vol%) and biotite (5 vol%). The matrix (65% fine crystalline) consists of K-feldspar (30–35 vol%), plagioclase (20–25 vol%)

and quartz (45 vol%) (Figure 5d). It formed at 182 ± 1 Ma (zircon U-Pb age), consistent with the mineralization age (179.6 ± 3.6 Ma) (molybdenite Re-Os age), within errors (to be published). In addition, the main ore-forming granite intrusion was not found in the drill cores below the main ore body of the K exploration line (Figure 2b). Although located at the edge of the main ore body, the granite porphyry develops weak silicified alteration, with magnetite–hematite–anhydrite–veins surrounding it (Figure 4b). Therefore, the granite porphyry dike could be a small branch of the ore-forming intrusion.

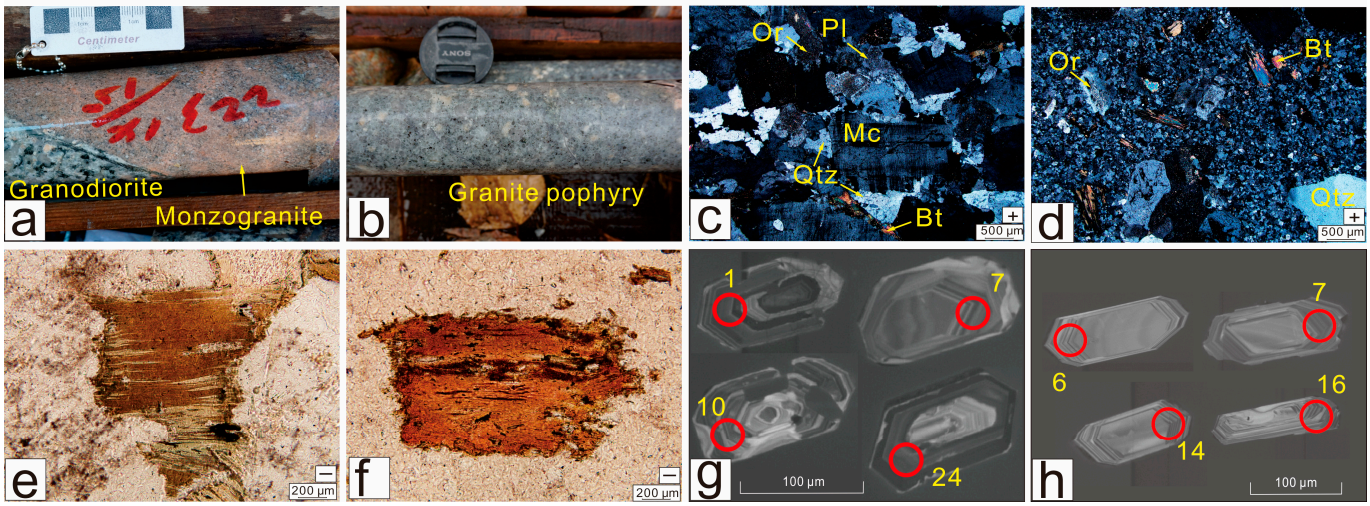

Figure 5. Photographs and photomicrographs of samples, including hand specimens of (**a**) monzogranite and (**b**) granite porphyry; photomicrographs of (**c**) monzogranite and (**d**) granite porphyry; photomicrographs of biotite of (**e**) monzogranite and (**f**) granite porphyry; cathodoluminescence photos of zircons of (**g**) monzogranite and (**h**) granite porphyry with some LA-ICP-MS test points represented by red circles. Abbreviations: Qtz = quartz; Bt = biotite; Or = orthoclase; Mc = microcline; Pl = plagioclase.

3.2. Fluid Inclusion Petrography

Fluid inclusions are abundant in quartz from all mineralization stages, but there are limited fluid inclusion assemblages (FIAs: [47]). Some fluid inclusions have negative crystal or oval shapes and may be primary in origin, while others have irregular shapes or are aligned along micro-fractures and are likely secondary or pseudosecondary. Only primary and pseudosecondary fluid inclusions are classified and measured in this study. Based on the phase compositions at room temperature and the homogenization behavior during heating, three types of fluid inclusions were recognized: vapor-rich (V-type), liquid-rich (L-type) and halite-bearing (H-type) (Figure 6).

The V-type fluid inclusions (Figure 6b,d,f,g) are widespread in the Stage 1–4 veins but are scarce in the Stage 5 veins. They are generally 6–18 μm long and have relatively high vapor phase volumetric proportions (40–100 vol.%). They homogenize to the vapor phase upon heating. The phase transitions are quite subtle to observe when the vapor phase is up to 70 vol.%, so the microthermometric results only include those with vapor phases < 70 vol.%, for the sake of accuracy.

The most common fluid inclusions at 460 Gaodi belong to the L-type (Figure 6), and consist of a vapor bubble and a liquid phase and are 3–20 μm long. The liquid proportions of the liquid phase usually range from 40 to 90 vol.% in the Stage 1–2 veins, whereas Stage 3–5 veins have higher liquid-phase proportions (40 to >90 vol.%). Upon heating, they homogenize to liquid by the disappearance of the vapor.

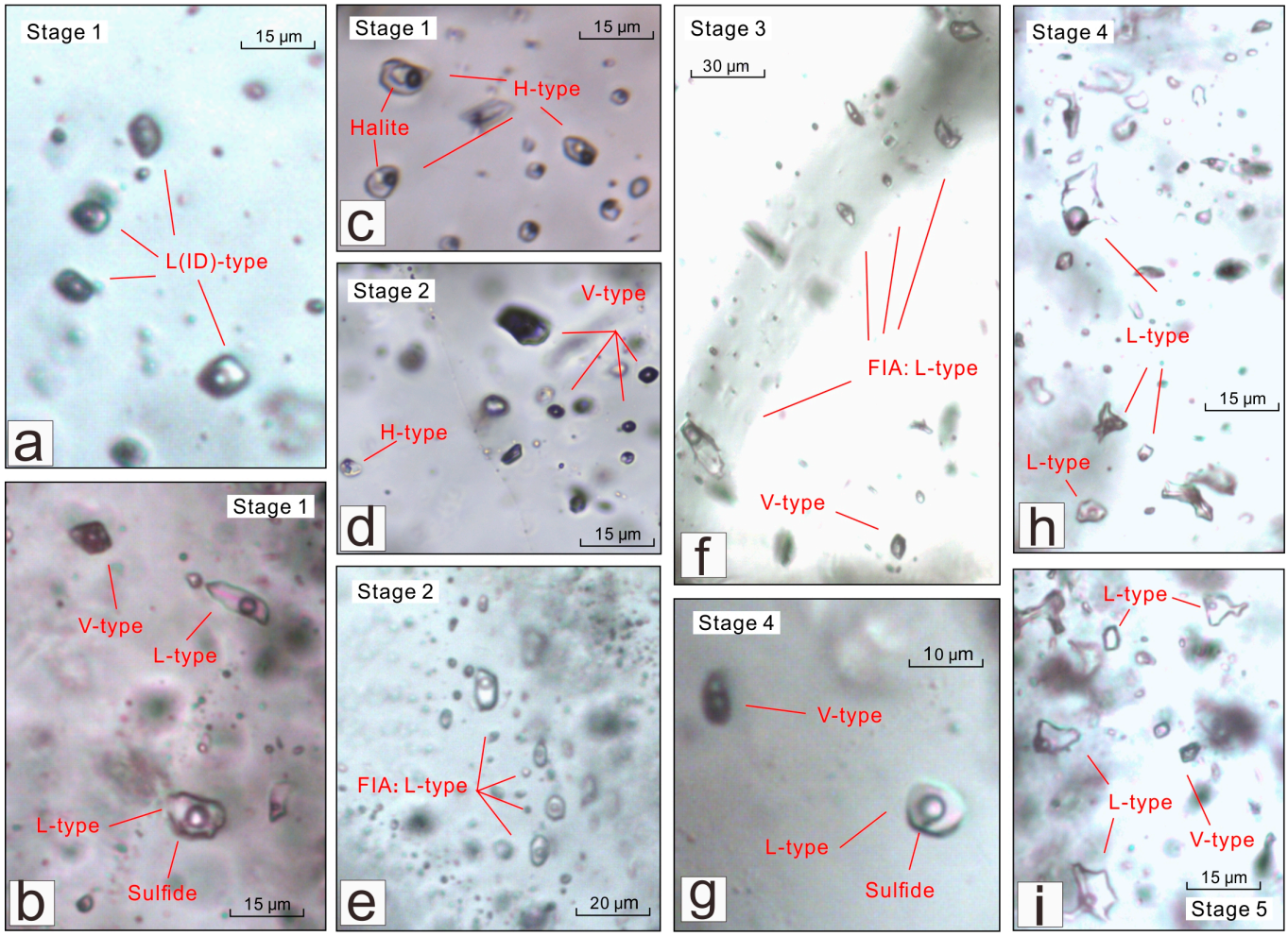

Figure 6. Photomicrographs of various types of inclusions in various hydrothermal stages of the 460 Gaodi deposit. (**a**) L (ID)-type inclusions in Stage 1; (**b**) L and V-type inclusions in Stage 1; (**c**) H-type inclusions in Stage 1; (**d**) H and V-type inclusions in Stage 2; (**e**) L-type FIAs in Stage 2; (**f**) L-type FIAs and V-type inclusions in Stage 3; (**g**) L and V-type inclusions in Stage 4; (**h**) L-type inclusions in Stage 4; (**i**) L-type inclusions in Stage 5.

The H-type inclusions (Figure 6c,d) consist of at least one cubic halite daughter mineral, a vapor bubble and a brine liquid phase. Other daughter minerals may include rounded sylvite, needle-like rutile and unidentified opaque metal minerals (Figure 6b,g). This kind of inclusion is usually observed in Stage 1–2 veins. All of the H-type inclusions analyzed have the homogenization mode in which vapor bubbles disappear first, followed by the exsolving of the halite daughter minerals at higher temperatures. This homogenization behavior may result from the accidental entrapment of halite [48] or post-entrapment modification [49]. Thus, the formation conditions of the veins cannot be constrained by the halite-bearing inclusions (H-type) and only the results from two-phase liquid-rich or vapor-rich inclusions were used to constrain the physicochemical conditions of the ore fluids.

3.3. Methods

3.3.1. Electron Microprobe Analysis of Biotite

Biotites from one monzogranite sample (3M-112) and two granite porphyry samples (8G-994 and 8G-997) were selected to carry out electron probe micro-analysis (EPMA). The EPMA study was completed at the Institute of Geology and Geophysics, Chinese Academy of Sciences (IGGCAS, Beijing, China), using a JEOL-JXA8100 electron microprobe. The

microprobe was operated at an accelerating voltage of 15 kV, a beam current of 20 nA, and a beam size of 5 μm. Matrix corrections were performed using the ZAF (Z: atomic number; A: absorption; F: fluorescence) correction program supplied by the instrument manufacturer.

3.3.2. Trace Elements of Zircon

A monzogranite sample (3M-112) and a granite porphyry sample (8G-994) were selected to analyze the trace elements of zircon. This experiment was carried out in conjunction with zircon U-Pb dating. All procedures of the test were completed at Beijing GeoAnalysis CO., LTD. (Beijing, China).

Zircon grains with intact crystal form, high transparency, few inclusions and few cracks were selected using conventional heavy liquid and magnetic techniques, and then hand-picked under a binocular microscope. Analytical spot locations were selected on the basis of cathodoluminescence (CL), backscattered electron imaging (BSE) and plane polarized light photography. The zircon CL image was taken using a high-resolution thermal field emission spectroscopy cathodoluminescence chamber under an operating power of 15 kV and 4nA. The NWR193UC model laser ablation system (Elemental Scientific Lasers LLC, Bozeman, MT, USA) was coupled to an Agilent 7900 ICP-MS (Agilent, Santa Clara, CA, USA). Detailed tuning parameters can be found in [50]. The analysis was performed using 30 μm diameter spots at 6 Hz and a fluence of 5 J/cm^2. The Iolite software package was used for data reduction [51]. Zircon GJ-1 and 91500 were used as primary and secondary reference materials, respectively. After every 10 analyses of the sample, 91500, GJ-1 and Plesovice were analyzed twice. Typically, 45 s of the sample signals were acquired after 25-s gas background measurements, using the exponential function to calibrate the downhole fractionation [51].

3.3.3. Fluid Inclusion Microthermometry

The microthermometry of the fluid inclusions was measured using a Linkam THSMG-600 stage equipped with a Leitz microscope at the IGGCAS. The measurement range of this cooling–heating system is from −195 °C to +600 °C. The system was calibrated using synthetic fluid inclusion standards (SynFlinc). The heating/freezing rate was 0.2–5 °C/min and was kept at 0.2 °C/min, near the phase transitions. The measurement uncertainties were ±0.2 °C and ±2 °C for temperatures below 30 °C and in the range of 30–600 °C, respectively.

4. Results

4.1. Biotite Composition

Results of electron-microprobe analyses of biotite from the monzogranite and granite porphyry samples are listed in Table S1 and summarized in Table 1.

The biotite phenocrysts are yellowish-brown with a well-defined crystal form and pronounced pleochroism, characteristic of magmatic biotite [52]. The grains analyzed in this study exhibit elevated TiO_2 content (2.68–3.23 wt% and 2.52–3.67 wt%, respectively), consistent with the magmatic biotite documented by [53,54]. Additionally, all biotite grains are either Ca-free or Ca-poor (Table 1) and display relatively homogeneous $Fe^{2+}/(Fe^{2+} + Mg^{2+})$ ratios (0.15–0.39), indicating minimal alteration by sericitization through post-magmatic deuteric processes [55,56].

Biotite from the monzogranite and granite porphyry has high MgO content (3M-112: 14.07–18.68 wt%; 8G-994/997: 12.26–14.28 wt%) and Al_2O_3 content (3M-112: 16.76–18.35 wt%; 8G-994/997: 14.86–18.78 wt%), but varied FeO content (3M-112: 5.62–11.48 wt%; 8G-994/997: 14.47–16.64 wt%). In the FeO^T–Al_2O_3–MgO diagram (Figure 7a), biotite from monzogranite falls within the Mg-biotite region, whereas biotite from granite porphyry falls within the Fe-biotite region.

Table 1. Some important results and parameters of electron-microprobe analyses of biotite.

Lithologies	STAT	SiO_2	TiO_2	Al_2O_3	FeO	MnO	MgO	CaO	Na_2O	K_2O	Cr_2O_3	NiO	F	Cl	Total	Al^T	$Fe^{2+}/(Mg+Fe^{2+})$	T °C	P (MPa)	Depth (km)
Monzo-granite (n = 13)	Min.	34.84	2.68	16.76	5.62	0.60	14.07	0.06	0.16	9.89	0.06	0.00	1.51	0.04	92.17	2.99	0.15	713	254	9.41
	Max.	39.18	3.23	18.35	11.48	0.79	18.68	0.21	0.34	10.99	0.13	0.04	2.49	0.11	99.46	3.09	0.31	786	284	10.52
	Avg.	37.72	2.90	17.70	7.91	0.69	16.82	0.10	0.27	10.70	0.09	0.01	1.93	0.06	96.89	3.05	0.21	759	270	9.99
	S.D.	1.36	0.19	0.38	2.03	0.08	1.48	0.04	0.06	0.28	0.03	0.01	0.28	0.02	2.08	0.03	0.06	23	10	0.36
Granite porphyry (n = 16)	Min.	32.73	2.52	14.86	14.47	0.24	12.26	0.03	0.12	6.79	0.02	0.00	0.77	0.01	91.80	2.69	0.33	677	161	5.97
	Max.	37.40	3.67	18.78	16.64	0.41	14.28	0.14	0.40	10.32	0.23	0.06	1.03	0.08	97.72	3.31	0.39	734	349	12.94
	Avg.	35.94	3.30	16.64	15.36	0.30	13.48	0.07	0.21	9.03	0.10	0.01	0.93	0.05	95.43	2.96	0.35	719	245	9.07
	S.D.	1.32	0.35	0.92	0.67	0.04	0.54	0.03	0.07	1.22	0.06	0.02	0.08	0.01	1.62	0.17	0.02	17	51	1.90

Structural formula is based on 8 cations, and 22 oxygen atoms. The number of Fe^{2+} and Fe^{3+} were calculated following the machine learning method from [57]. The temperatures are calculated after Ti-in-biotite thermometer T(°C) = {[ln(Ti) + 2.3594 + 1.7283 × $(X_{Mg})^3$]/4.6482 × 10^{-9}}$^{0.333}$, X_{Mg} = 0.275~1.000, Ti = 0.040~0.600, T = 400~800 °C [58]. The pressures are calculated after biotite barometer P(kbar) = 3.03 × Al^T − 6.53(±0.33) [59]. Depth (km) means paleodepth calculated from P = ρgH (ρ = 2700 kg/m^3, g = 9.8 m/s^2).

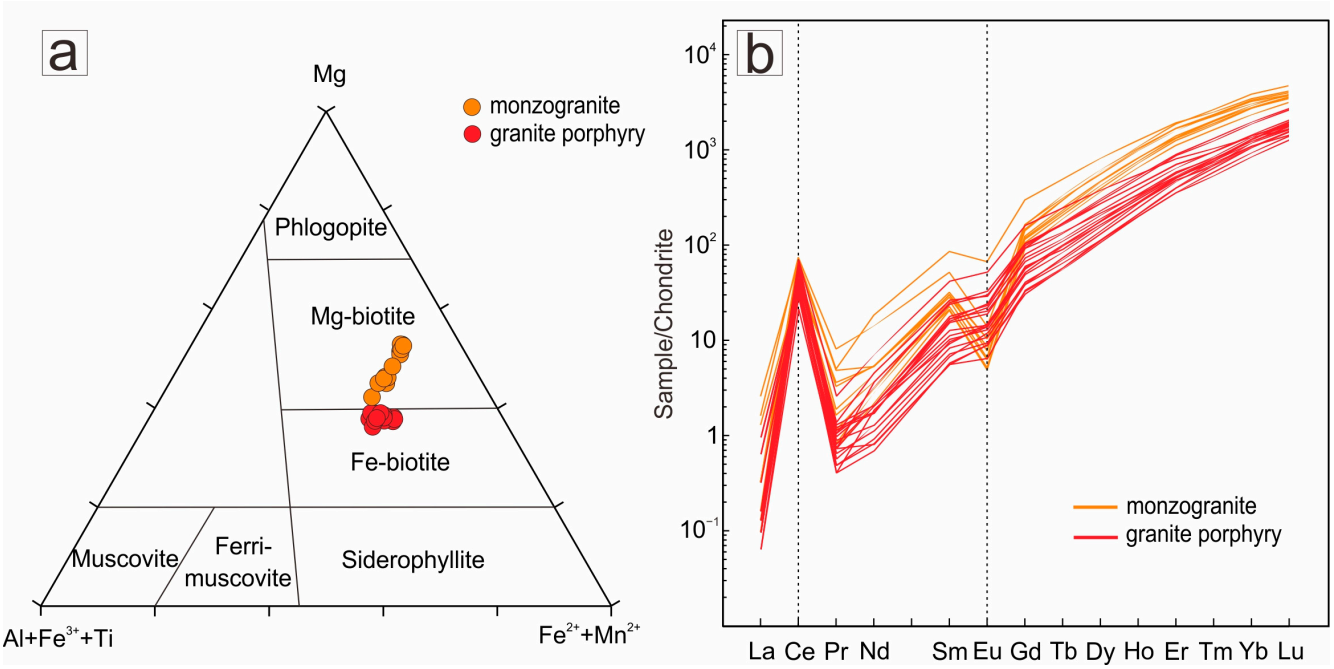

Figure 7. (**a**) Classification diagram of biotite, modified after [60] and (**b**) Chondrite-normalized REE patterns of zircons (normalized values after [61]).

4.2. Zircon Geochemistry

Trace element data (ppm), and parameters of the granitoids in the 460 Gaodi Mo-Cu deposit are presented in Table S2 and summarized in Table 2.

Table 2. Data summary of zircon trace elements and calculated parameters (ppm).

Lithologies	Statistics	Ti	Ce	Eu	ΣREE	LREE/HREE	Eu/Eu*	lg(fO_2)	T(°C)	$(Ce/Ce^*)_D$	Ce^{4+}/Ce^{3+}	ΔFMQ
3M-112 (n = 10)	Min.	2.2	24.20	0.36	1107	0.02	0.14	−18.2	659	15.0	14.0	−2.5
	Max.	5.7	60.20	4.92	1883	0.05	0.60	−12.8	741	122.7	121.8	4.1
	Avg.	3.6	41.94	1.04	1491	0.04	0.23	−15.5	696	67.2	66.3	1.3
	S.D.	1.2	13.63	1.38	250	0.01	0.13	1.8	27	33.2	33.2	2.0
8G-994 (n = 20)	Min.	1.5	17.40	0.48	409	0.04	0.45	−14.0	630	49.1	48.2	1.8
	Max.	5.7	57.10	3.88	971	0.12	0.72	−7.9	741	649.9	649.7	9.6
	Avg.	3.1	36.11	1.41	633	0.07	0.58	−10.6	684	300.3	299.7	6.6
	S.D.	1.1	12.07	0.81	154	0.02	0.06	1.7	28	151.2	151.4	1.9

In this study, lg(fO_2), T(°C), Ce^{4+}/Ce^{3+}, $(Ce/Ce^*)_D$ and ΔFMQ are calculated using the software Geo-fO_2 [62]. In this software, T(°C) is calculated by the revised Ti-in-zircon thermometer [63,64] ($aSiO_2$ = 1, $aTiO_2$ = 0.6). The lattice-strain model (LSM) [65] is used to estimate zircon Ce anomalies. $(Ce/Ce^*)_D$ was therefore set at $(Ce/Ce^*)_D = (Ce/Ce^*)_{LSM}$ for Ce anomalies. The Ce^{4+}/Ce^{3+} ratio is obtained by calculating Ce^{4+} and Ce^{3+} separately, using the LSM [66].

CL image show that most zircon is short columnar, followed by long columnar, with a euhedral–subhedral granular texture. The crystal edges and cone tops of a few zircons are eroded, the surface is clean, and has typical magmatic growth oscillation zones and rhythmic texture (Figure 5g,h), which indicates magmatic origin. In addition, almost all spots have Th/U values greater than 0.4, suggesting a typical magmatic zircon feature [67]. The granularity of zircons is mostly 100–200 μm in size, and aspect ratios of most columnar crystals are 1.2–1.8.

All zircon samples from the monzogranite and granite porphyry show strong positive Ce anomalies, intermediate-to-strong negative Eu anomalies (Eu/Eu* = 0.14–0.72), and significant enrichment of heavy rare earth elements (HREE) (LREE/HREE = 0.02–0.12) (Figure 7b, Table 2). These trace element patterns and ∑REE abundances of 409 to 1883 ppm are typical of igneous zircons (~250–5000 ppm; [68]).

4.3. Fluid Inclusion Microthermometry

Microthermometry results are presented in Table S3 and summarized in Table 3. Frequency distribution histograms of the homogenization temperature and salinity of fluid inclusions in different stages are shown in Figure 8.

Table 3. Fluid inclusion types and their microthermometric results.

Stage	Types	Statistics	Liquid Proportion	Tm/°C	Th_{halite}/°C	Th_{L-V}/°C	Th/°C	Salinity [1]	Pressure/MPa [2]
1	V (n = 31)	Min.	35	−8.3			238	3.4	19.5
		Max.	60	−2.0			450	12.0	48.3
		Avg.	50	−4.9			372	7.6	35.3
	L (n = 58)	Min.	40	−8.6			240	4.2	21.5
		Max.	80	−2.5			482	12.4	53.1
		Avg.	60	−5.3			366	8.2	35.5
	H (n = 12)	Min.			419	191	419	49.5	
		Max.			476	311	476	56.6	
		Avg.			453	258	453	53.7	
2	V (n = 31)	Min.	40	−7.1			260	3.1	20.1
		Max.	60	−1.8			430	10.6	42.2
		Avg.	53	−4.6			340	7.2	31.6
	L (n = 77)	Min.	40	−7.8			245	4.0	21.2
		Max.	90	−2.4			458	11.5	47.2
		Avg.	66	−5.2			345	8.1	33.3
	H (n = 12)	Min.			300	166	300	38.1	
		Max.			407	312	407	48.2	
		Avg.			358	231	358	43.3	
3	L (n = 122)	Min.	60	−7.1			144	3.2	12.4
		Max.	>90	−1.9			383	10.6	38.1
		Avg.	76	−4.3			248	6.8	22.7
4	V (n = 22)	Min.	30	−3.9			157	3.4	12.6
		Max.	60	−2.0			250	6.3	21.6
		Avg.	47	−3.3			190	5.4	16.1
	L (n = 84)	Min.	40	−5.9			115	3.8	9.0
		Max.	>90	−2.3			310	9.1	30.7
		Avg.	78	−4.1			223	6.5	20.2
5	L (n = 86)	Min.	60	−6.0			121	3.5	9.9
		Max.	>90	−2.1			246	9.2	24.2
		Avg.	88	−3.7			170	6.0	15.0

[1] Salinities of aqueous fluid inclusions, expressed as wt.% NaCl equiv., were estimated using formulas by [69], in which salinities of halite-bearing inclusions were estimated on the basis of the melting temperatures of the halite crystals. [2] The fluid pressure is estimated on the basis of empirical formulas by [70].

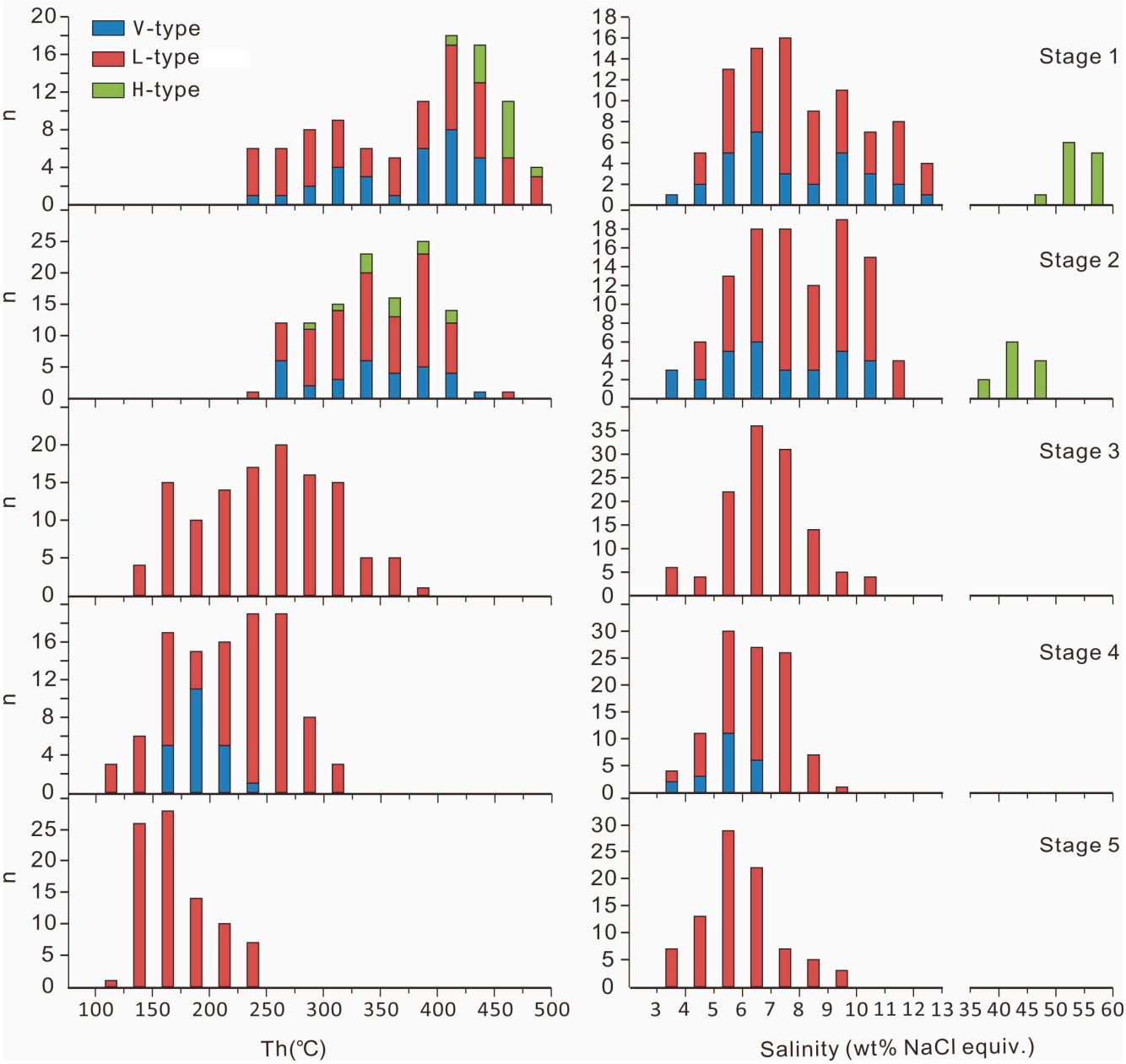

Figure 8. Frequency distribution histograms of homogenization temperature and salinity of fluid inclusions in different stages of the 460 Gaodi deposit.

For Stage 1 veins, the final ice-melting temperatures of V-type inclusions ranged from −2.0 to −8.3 °C, corresponding to salinities of 3.4 to 12.0 wt% NaCl equiv. These inclusions homogenized to the vapor phase at temperatures of 238 to >450 °C. The final ice-melting temperatures of L-type inclusions from Stage 1 veins spanned from −2.5 to −8.6 °C, with calculated salinities of 4.2–12.4 wt% NaCl equiv. (Table 3). These inclusions homogenized to the liquid phase at temperatures of 240 to >482 °C (Table 3). Both V-type and L-type inclusions exhibited low to moderate salinities. All H-type inclusions homogenized to liquid following the disappearance of vapor bubbles during heating. Halite dissolving temperatures ranged from 419 °C to 476 °C, with vapor bubbles disappearing between 191 °C and 311 °C. Relatively high salinities of 49.5–56.6 wt.% NaCl equiv. were calculated from halite-dissolving temperatures.

The fluid inclusion types, salinities and homogenization temperatures from the Stage 2 veins are similar to those from the Stage 1 veins, but with relatively low absolute values

(Figures 6b–e and 8). The V-type and L-type inclusions show salinities of 3.1 to 10.6 wt% NaCl equiv. and 4.0–10.5 wt% NaCl equiv., respectively. The homogenization temperatures for the V-type and L-type inclusions range from 260 to 430 °C and 245 to 458 °C, respectively (Table 3). The H-type inclusions have Th_{L-V} and Th_{halite} ranging from 166 to 312 °C and from 300 to 407 °C, respectively (Table 3). The corresponding salinities range from 38.1 to 48.2 wt% NaCl equiv.

The V-type inclusions observed within the Stage 3 veins are either too small or too subtle to observe the phase transitions to perform a microthermometry analysis; thus, only the well-developed L-type inclusions are measured. They have relatively lower salinities (3.2–10.6 wt% NaCl equiv.) and homogenization temperatures (144–383 °C) compared to the Stage 1–2 inclusions.

The fluid inclusions within the Stage 4 veins are dominated by V-type and L-type inclusions with high liquid proportions, showing low calculated salinities of 3.4–6.3 wt% NaCl and 3.8–9.1 wt% NaCl equiv., respectively, and low homogenization temperatures of 157–250 °C and 115–310 °C.

The L-type inclusions are the only type in the Stage 5 veins, and are generally of an irregular shape, with the highest liquid-phase proportion (60% to >90%). They homogenized to liquid between 121 °C and 246 °C. Ice-melting temperatures are between −2.1° and −6.0 °C, with corresponding salinities between 3.5 and 9.2 wt% NaCl equiv., showing the lowest absolute values (Figure 8).

5. Discussion

5.1. Magmatic Conditions

5.1.1. Temperature

The Ti content in biotite is sensitive to temperature changes and can be used to estimate the crystallization temperature of biotite [58]. The Ti-in-biotite thermometer [58] gave crystallization temperatures of biotite in monzogranite from 713 to 786 °C (average 759 °C), and those of biotite from granite porphyry from 677 to 734 °C (average 719 °C) (Table 1, Figure 9a).

Ti can substitute for Zr^{4+} and Si^{4+} in zircon, and the crystallization temperature of zircon has certain constraints on Ti content and element substitution [71,72]. Therefore, the Ti-in-zircon can be used to calculate the saturation temperature of zircon. Because the Ti-in-zircon temperature is also affected by the activity of SiO_2 and TiO_2, the revised Ti-in-zircon thermometer was utilized to calculate the temperature of the melt during zircon crystallization [63,64] ($aSiO_2$ = 1, $aTiO_2$ = 0.6). The Ti-in-zircon temperatures of monzogranite range from 659 to 741 °C (average of 696 °C), and those of granite porphyry range from 630 to 741 °C (average of 684 °C) (Table 2).

The crystallization temperatures of biotite exceed those of zircon, potentially indicating either earlier crystallization of biotite relative to zircon or a broader crystallization temperature range resulting from more extensive magma differentiation. The crystallization temperatures of monzogranite, as determined by two mineral thermometers, are higher than those of granite porphyry. This may be attributable to the more mafic composition of monzogranite or the higher water content of granite porphyry.

5.1.2. Pressure and Crystallization Depth

The Al^T (Al^{VI} + Al^{IV}) of biotites from the monzogranite and granite porphyry is 2.99–3.09 apfu (atoms per formula unit) and 2.69–3.31 apfu, respectively (Table 1). The Al^T content of biotite can be used to estimate the solidification pressure (P) of the granitic rocks, based on Le Chatelier's principle [59]. The solidification pressure is estimated as 254–284 MPa for monzogranite (average of 270 MPa). Depth can be estimated by the formula P = ρgH (ρ = 2700 kg/m^3, g = 9.8 m/s^2). Thus, the solidification depth of monzogranite (3M-112) ranges from 9.4 to 10.5 km (average of 10.0 km).

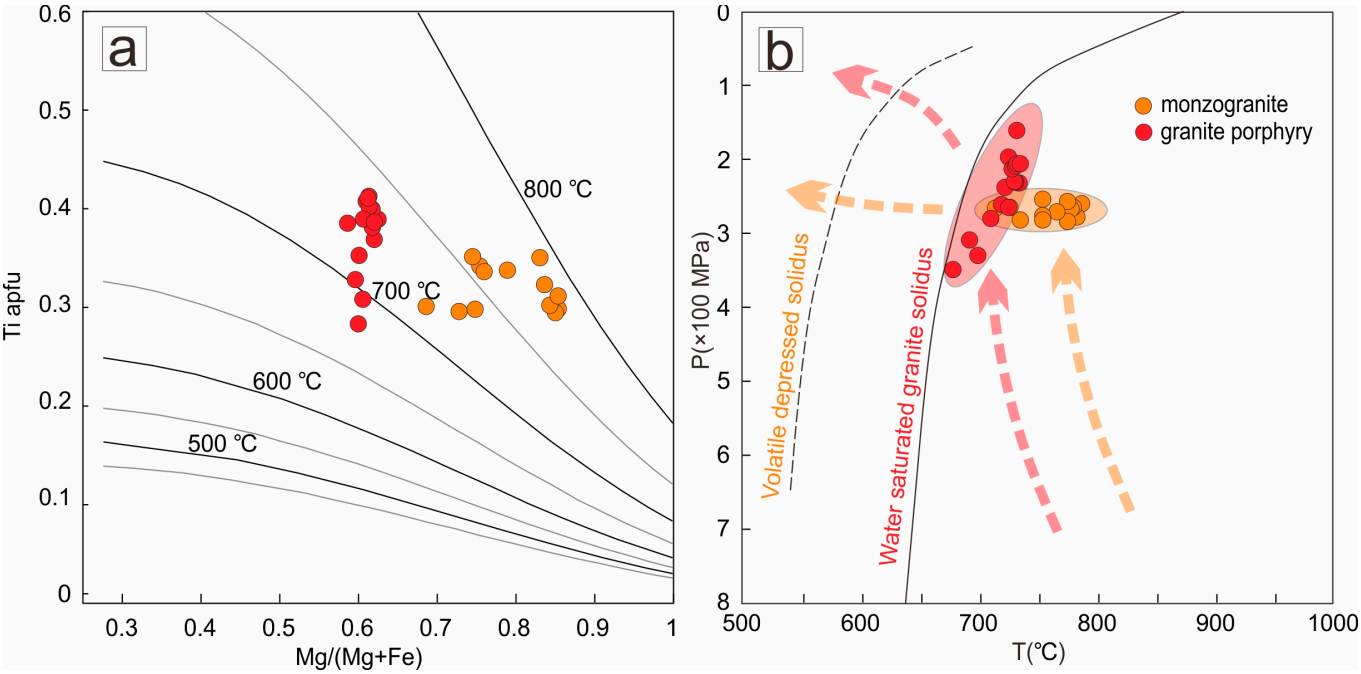

Figure 9. (**a**) Ti vs. Mg/(Mg + Fe) diagram, after [58]; (**b**) Approximate conditions for forming of granitic melts estimated by biotite, with the water-saturated granite solidus curve after [73] and the volatile depressed-solidus curve after [74].

However, for the granite porphyry (8G-994), the pressure of 161–349 MPa (average of 245 MPa) calculated by biotite phenocryst can be much higher than the porphyry emplacement pressure, since the phenocrysts usually crystallize in the upper-crust magma chamber [75,76], in which the composition of biotite was related to the chemical equilibrium during crystallization [76]. Therefore, the pressure range should be that of the parental chamber of the porphyry, corresponding to a depth of 6.0 to 12.9 km.

Furthermore, when the temperature and pressure data obtained from biotite in the two lithologies are plotted in a P-T diagram for the approximate conditions of granitic melt formation (Figure 9b), notable differences emerge. The consolidation pressure obtained from biotite in monzogranite displays a narrow range of variation, while its crystallization temperature exhibits a broad range. This suggests that during the transition from biotite crystallization to monzogranite consolidation, the magma ceased its ascent (maintaining a constant pressure) and underwent a gradual cooling process. If the granite is water-unsaturated, it may undergo lateral evolution and intersect with the volatile depressed solidus, resulting in crystallization. Hence, in Figure 9b, the P-T value of biotite in monzogranite is depicted as the P-T condition when the magma intrudes into the consolidation position, but the biotite is still undergoing crystallization. Similarly, for ore-related granite porphyry, the pressure value of its porphyritic biotite is confined to the P-T state, corresponding to the crystallization of biotite in the deep (multi-level or otherwise) parent magma chambers, with a vast range of depths, as evidenced by its wide range of temperature and pressure values.

5.1.3. Redox State

In this study, based on Ti-in-zircon temperatures, a zircon oxybarometer based on the zircon Ce anomaly [77] was used to determine the redox state of magmas. The lattice-strain model [65] was used to estimate zircon Ce anomalies. For comparison, magma redox states were also calculated from zircon Ce^{4+}/Ce^{3+} ratios, using the lattice-strain model [66]. All the above methods are integrated into the software Geo-fO_2 [62]. As the presence of REE-bearing minerals may affect both the deviation from the lattice-strain model (if crystallized before zircon) and the REE composition of zircon (if present in undetected

inclusions) [78], inclusion-free and clean zircons (La $\leq$ 0.1 ppm) are used for calculations of oxygen fugacity.

Zircons from monzogranite (3M-112) show low zircon lg(fO_2) values, with ΔFMQ ranging from −2.5 to +4.1 (average +1.3; where ΔFMQ is the lg(fO_2) deviation from the FMQ buffer). Comparatively, granite porphyry (8G-994) has high zircon lg(fO_2) values, with ΔFMQ ranging from +1.8 to +9.6 (average +6.6). The average Ce^{4+}/Ce^{3+} ratios of zircons from the monzogranite and the granite porphyry are 66.3 and 299.7, respectively (Table 2). On zircon lg(fO_2) vs. temperature (Figure 10a), the ore-related granite porphyry sample is much more oxidized than the barren monzogranite.

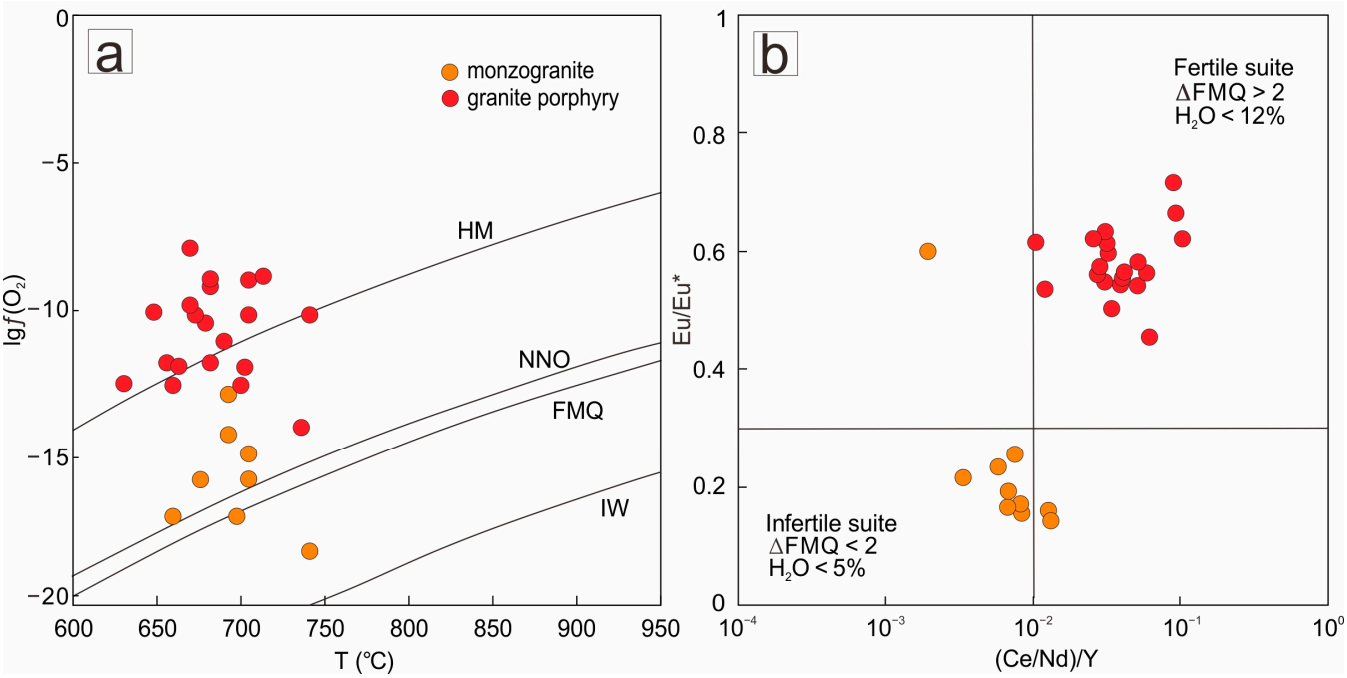

Figure 10. (**a**) Zircon lg(fO_2) vs. temperature, after [77]; (**b**) Zircon trac-element ranges to define high oxygen fugacity–high water content fertile magma (ΔFMQ > 2 and H_2O < 12%) and low oxygen fugacity–low water content (ΔFMQ < 2 and H_2O < 5%) infertile suite refer to [79]. HM: magnetite-hematite buffer curve; NNO: Ni-NiO buffer curve; FMQ: fayalite-magnetite-quartz buffer curve; IW: iron-wustite buffer curve.

During the crystallization process of magma, the high oxygen fugacity of magma will stabilize S as SO_4^{2-} and inhibit the sulfide saturation, which could scavenge copper and gold [11,80,81]. The Mo/W ratio in magmatic hydrothermal deposits should increase as the oxygen fugacity of the magma increases, due to the effect of oxygen fugacity on the sequestering of Mo vs. W [28]. This indirectly increases the content of ore-forming elements such as Mo, Cu and Au in melts and subsequent exsolved fluids. Therefore, granite intrusions with high oxygen fugacity are more fertile for Mo-Cu-Au than reduced ones.

A few other effective fertility indicators for zircons from granites are Eu/Eu* and (Eu/Eu*)/Y ratios. The distinctive zircon ratios in the fertile suites are interpreted as indicating an extremely high magmatic water content and high oxidation states [79]. The zircon datapoints of the granite porphyry plot are within the fertile region represented by high oxygen fugacity–high water content magma (Figure 10b), which proves from another perspective that granite porphyry is more favorable for mineralization than monzogranite.

5.2. Crystallization, Supercritical Fluid, and Exsolving Depth

Typically, shallow-level porphyry stocks are diminutive in size and do not generate the majority of the magmatic fluid volume. Instead, they serve as "exhaust valves" or conduits for the upward transmission of fluids from parental magma chambers located at the greater depths of 1 to 3 km or more, corresponding to paleodepths of 5 to 15 km [82–84]. These chambers also function as supply sources for both the magmas that form the porphyry stocks and the high-pressure metalliferous fluids, potentially via cupolas on their roofs which represent the key areas of the hydrothermal system [82]. Observations have revealed the development of coarse muscovite veins and alteration at the "root zone" at paleodepths of approximately 6–7 km [84,85], demarcating the lower boundary of the porphyry deposit system [86]. The sudden and voluminous release of volatiles typically occurs concurrently with the emplacement of porphyry intrusions [84,87]. Notably, the depth of the upper portion of the magma chamber, which also represents the fluid-exsolving depth, may exert a significant influence on the composition and behavior of volatile compounds precipitated during crystallization and on the characteristics of the deposit [36].

Studies have revealed that the primary constraint on the depth of magma emplacement in association with hydrothermal deposits lies in the conduct of H_2O within the magma [88]. The solubility of water in granite is greatly influenced by pressure. As pressure decreases, water solubility drops, thus facilitating the saturation of granite with water, leading to the exsolving of supercritical fluids [89]. The initial H_2O content of magma linked to extensive hydrothermal activity ranges from 2.5 to 6.5wt% [88]. The zircon datapoints of granite porphyry evince the high water content of the original magma (Figure 10b). In Figure 9b, it is postulated that the point at which the water-rich magma ascends to the solidus of water-saturated granite denotes the depth of the exsolving supercritical fluid [73].

Interestingly, in Figure 9b, the crystallization pressure–temperature (P-T) range of the aforementioned phenocryst biotite from the granite porphyry lies precisely below the solidus of water-saturated granite. This observation implies that the entire process of biotite crystallization is concomitant with the subsequent fluid exsolving. Therefore, the two aforementioned events of biotite crystallization and fluid exsolving occur simultaneously, in both time and space. The minimum crystallization pressure of biotite, estimated to be around 6 km, can constrain the minimum depth of fluid exsolving. This depth corresponds to the upper limit of the parent magma chamber and marks the lower boundary of the porphyry hydrothermal system.

5.3. Fluid Evolution Process in the Hydrothermal Stage

5.3.1. Estimation of Temperature and Pressure of Hydrothermal Stages

As mentioned earlier, the formation conditions of veins cannot be constrained by the homogenization temperatures of the halite-bearing inclusions (H-type) in this 460 Gaodi deposit. In addition, despite the presence of halite-bearing inclusions and low salinity V-type inclusions, there are few observed presences of typical fluid boiling in the Stages 1–2 veins (Figure 6a–e), of which the representative feature is the coexistence of H-type inclusions and L/V-type inclusions of various liquid-phase proportions, sharing similar homogenization temperatures (Figure 8). Hence, the boiling inclusion-pressure measurement method is unavailable here. Only data from L-type and V-type inclusions can be used to estimate the fluid-trapping P-T conditions.

For the H_2O-NaCl system, the trapping temperatures of V/L-type fluid inclusions are higher than the homogenization temperatures. Thus, to minimize errors, we set the average homogenization temperature as the lower limit of the trapping conditions and the highest homogenization temperature as the upper limit, referring to a previous case study [90]. The trapping pressures of the inclusions are estimated based on empirical formulas by [70]. The P-T conditions based on these methods are roughly constrained.

In addition, the Stage 1–2 veins contain a few intermediate-density (ID) fluid inclusions (Figure 6a), with average salinities of 10.1–12.4 wt% NaCl equivalent. The homogenization occurred by expansion of the bubble to the vapor phase (V-type) or the disappearance of the

bubble to the liquid phase (L-type) at temperatures of 397 to 480 °C, with consistent vapor bubble proportions (40–80 vol.%), at room temperature. This fluid inclusion is generally believed to be the residual initial fluid after exsolving from magma, preserved in the deep part of many porphyry deposits [91–93]. Although there is significant overlap between these ID-type fluid inclusions and the P-T conditions of the Stage 1–2, it is evident that, due to preserving conditions, there will be many ID-type inclusions with higher temperatures at depth.

Utilizing the aforementioned conditions, we derived the pressure–temperature (P-T) conditions for each stage (Table 4). As the fluid stage progresses, there is a concomitant decrease in both temperature and pressure, suggestive of continuous cooling and ascent of the ore-forming fluids.

Table 4. The pressure–temperature (P-T) conditions for each fluid stage.

Stages	1	2	3	4	5
T(°C)	368–>482	343–458	248–383	216–310	170–246
P(MPa)	35–>53	33–37	23–38	19–31	15–24

5.3.2. Phase Change and Metal Precipitation Mechanisms

As depicted in Figures 8 and 11a and Table 3, inclusions from Stage 1–2 are predominantly characterized by L/V-type inclusions with liquid-phase proportions ranging from 35% to 80%, ID-type inclusions exhibiting high homogenization temperatures and intermediate salinity, and a paucity of H-type inclusions. In contrast, Stage 3–4 inclusions comprise primarily L/V-type inclusions, with liquid-phase proportions spanning 30% to over 90%, whereas Stage 5 inclusions consist solely of L-type inclusions exhibiting low salinity and high liquid-phase proportions (50%–90%). Notably, the main Mo mineralization is associated with Stage 2, while subordinate Mo-Cu mineralization is linked to Stage 4.

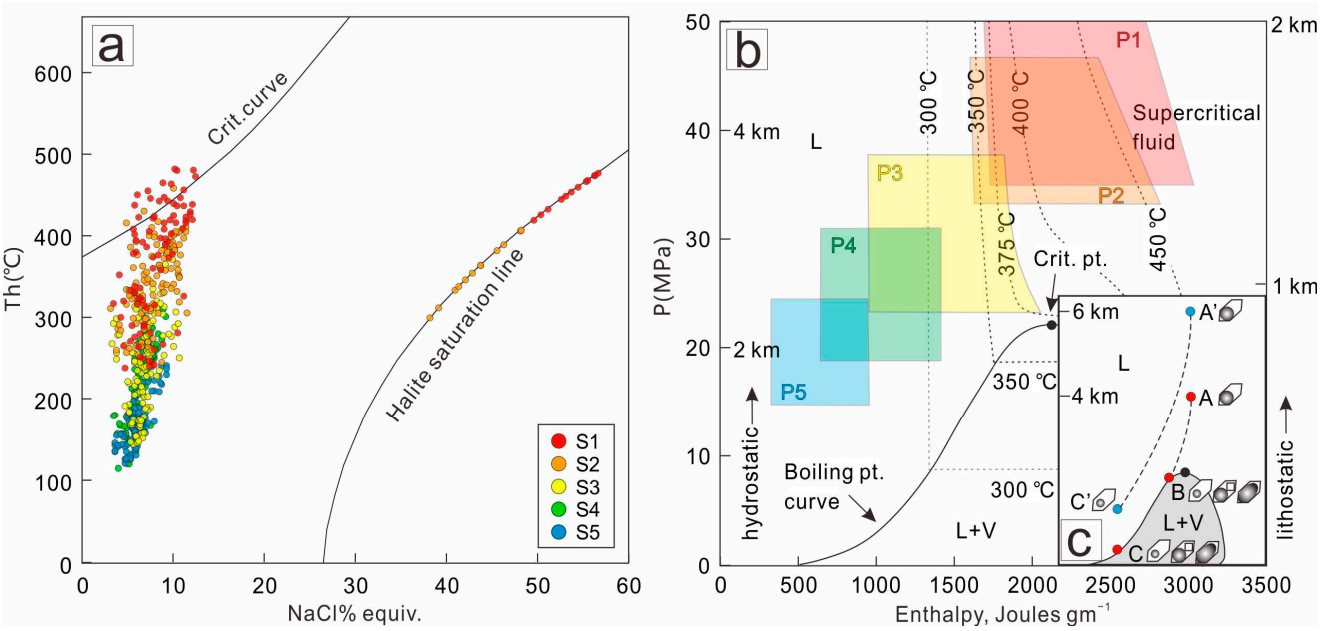

Figure 11. (**a**) Homogenization temperature vs. salinity diagram showing result of fluid inclusion microthermometry with NaCl saturation curve and critical point curve, after [94,95]; (**b**) Pressure–temperature evolution paths of different generations of 460 Gaodi deposit shown on pressure–enthalpy diagram, after [94,96]; (**c**) Simplified pressure–enthalpy diagram showing arrows indicating partly conductive (decreasing enthalpy with decreasing depth) cooling paths at different starting depth.

The identification of ID-type inclusions within the high-temperature range of Stage 1–2 implies the existence of initial single-phase fluids exhibiting intermediate density and supercritical properties at greater depths within the deposit. These fluids migrated upwards to a specific depth, whereupon a decrease in temperature and pressure facilitated the unloading of potassium from the fluids, resulting in the formation of K-feldspar and the biotite characteristic of Stage 1. As pressure continued to decrease during Stage 2, certain fluid P-T evolution paths may have intersected with the boiling-point curve, leading to partial phase separation, despite a lack of direct evidence. This resulted in the separation of the single-phase fluid into a low-salinity gas phase and a high-salinity liquid phase, accompanied by intense decompression. Given the pressure sensitivity of Mo solubility in solution, this boiling or fluid immiscibility precipitated a certain amount of Mo, forming a concentrated, columnar Mo main ore body, albeit at low grade. However, only some of the fluids underwent this process, with the remaining fluids still containing some Mo and most of the Cu. Subsequently, the temperature and pressure of the fluids that did not undergo phase transition decreased gradually, with their primary P-T evolution path failing to intersect with the boiling-point curve. These residual fluids experienced an increase in liquid proportion during cooling and a continuous decrease in salinity, due to precipitation of substances within the fluid. Following the precipitation of sericite and pyrite during Stage 3, Cu and Mo were precipitated from the liquid-rich fluid during Stage 4, as a result of a significant reduction in temperature (310–216 °C), conducive to Cu-Mo precipitation (Mo at 510–244 °C and Cu at 360–159 °C, based on some Cu-Mo porphyry deposits in NE China [97–99].

In summary, certain unboiled fluids from Stage 2, which would have exhibited high mineralization efficiency due to the effective decompression effect, retained ore-forming elements within the fluids until Stage 4. However, during Stage 4, the low cooling rate facilitated the dispersed precipitation of ore-forming elements as strip-shaped ore bodies that are challenging to mine. Consequently, the formation of the 460 Gaodi deposit, classified as a "sub-economic" deposit, is intimately linked to the "inefficient" fluid P-T evolution path, despite the fertility of its ore-forming granite porphyry, as previously discussed.

5.4. Fluid-Exsolving Depth and Mineralization Quality

When considering the impact of exsolving depth on mineralization, it is crucial to first examine the effect of varying fluid-exsolving depths, or pressures, on the distribution coefficients of the Cu, Mo, and S elements during the exsolving process [14]. This process determines the initial element content in the fluid, which directly affects the total amount of metal in the deposit. Cu is primarily present in the form of Cu-Cl complexes in fluids, and related to Cl contents [100,101]. However, the effect of pressure on the coefficient of Cl between the melt/fluid is complex, and not directly related [25,26,102,103]. Nonetheless, Cl is easily distributed in the fluid [100], so the influence of exsolving depth on the distribution of Cu and Cl elements may be negligible or difficult to discern. Mo also tends to enter the fluid [104], and as pressure increases, $D_{F/M}$ also increases [105,106]. Thus, increasing exsolving depth is beneficial for Mo to dissolve from the melt into the supercritical fluid. Additionally, high-pressure leaching fluids tend to have higher S content [27], which impacts the proportion of the S element in the deposit [36,99] and directly increases the content of minerals such as molybdenite and chalcopyrite, thereby promoting mineralization.

Overall, increasing exsolving depth is advantageous for the distribution coefficients of elements such as Cu, Mo, and S, and the initial ore-forming element content in the supercritical fluid. This is supported by the abundance of low-grade metal elements in the deposit, which suggests that while the deposit does not lack the total amount of metal, the degree of mineralization concentration is still poor. Therefore, it can be inferred that the P-T evolution process, the accompanying phase-transition process, and the metal precipitation mechanism of the dissolved supercritical fluid during the hydrothermal stage have a more significant impact on mineralization quality than the amount of metal carried by the dissolved fluid.

To further investigate the influence of depth on the sub-economic 460 Gaodi deposit, it is necessary to consider the conductive cooling of supercritical fluids following exsolution from magma and prior to ascent to the precipitation site. Accordingly, a pressure–enthalpy diagram (Figure 11b,c), which plots enthalpy against pressure for pure water and is contoured with selected isotherms, is employed to intuitively represent the process of heat conduction during fluid evolution [97,99]. A boiling curve located to the left of the critical point demarcates the liquid + vapor-phase zone below from the single-phase zone above, with a field of liquid water situated to the left of the boiling-point curve. As natural ore-forming fluids are aqueous solutions containing NaCl or CO_2, the range of curve traps may exhibit slight variations [97].

Fluids may exsolve from either the single-phase or two-phase zone, contingent upon the prevailing pressure. It is generally postulated that when the fluid-exsolving depth is less than 4 km (corresponding to a pressure of 130 MPa), the fluid exsolves from the two-phase zone, simultaneously releasing a high-salinity rich liquid phase and a low-salinity rich gas phase. Conversely, when the depth exceeds this threshold, the exsolved fluid is typically a low-salinity supercritical fluid [21,32,33].

An "economic" scenario is conceptualized as curve A-B-C in Figure 11c. In this scenario, the supercritical fluid exsolving from ore-forming porphyry at a crystallization depth of approximately 4 km at point A undergoes slight conductive cooling, in addition to decompressional cooling during its extended journey to the mineralization site. The fluid initially enters the liquid-only field before intersecting the two-phase field on the boiling-point curve at point B. Further decompression follows along the boiling-point curve, representing a favorable path for mineralization.

However, when the fluid-exsolving depth of ore-forming porphyry increases beyond 6 km, assuming that the initial enthalpy of the supercritical fluid remains constant and the rate of heat conduction is unchanged, the decompression path is likely to follow curve A'-C' in Figure 11c. This implies that, prior to reaching the optimal mineralization location, the fluid undergoes significant conductive cooling along the decompression path, resulting in a lower temperature at equivalent pressure. The initial supercritical fluid transitions into, and remains within, the liquid-only field without boiling during ascent to the mineralization sites. While it cannot be excluded that a small proportion of high-temperature liquids may still intersect the two-phase field on the boiling-point curve, this scenario represents a "sub-economic" situation in comparison to the aforementioned "economic" scenario.

The estimated P-T condition range of fluids at each stage of the 460 Gaodi deposit is depicted in Figure 11b. The decompression path followed by its initial supercritical fluid is likely represented by curve A'-C'. Based on the biotite barometer, the fluid-exsolving depth, approximately equivalent to the depth of the upper portion of the ore-forming magma chamber, exceeds 6 km. Furthermore, the fluid depth of Stage 1, as calculated using hydrostatic pressure, also indicates a depth greater than 5 km (Figure 11b). These findings are consistent with the aforementioned "sub-economic" scenario, in which it is difficult for fluids to boil and efficiently enrich metals. Consequently, the fluid-exsolving depth can exert a considerable impact on the mineralization quality of a porphyry deposit.

6. Conclusions

(1) The fluid-exsolving depth of the 460 Gaodi porphyry Mo-Cu deposit exceeds 6 km;
(2) The ore-related granite porphyry exhibits elevated zircon lg(fO_2) ratios, with ΔFMQ values ranging from +1.8 to +9.6 (average ΔFMQ of +6.6), indicative of high oxidation states and greater mineralization potential of the metallogenic magma, compared to pre-ore monzogranite;
(3) Owing to the considerable depth of fluid exsolution, a significant proportion of the fluid undergoes substantial conductive cooling along the slow decompression path, resulting in P-T conditions that remain within the liquid-only field without boiling, which favors metal enrichment;

(4) The fluid-exsolving depth can have a considerable impact on the mineralization quality of a porphyry deposit, and hence should be taken into account when evaluate the economic potential of mineral occurrences/deposits.

Supplementary Materials: The following supporting information can be downloaded at https://www.mdpi.com/article/10.3390/min13050699/s1, Table S1: Electron probe test results and related parameters of biotite; Table S2: Zircon LA-ICP-MS test results and related parameters; Table S3: Raw data of fluid inclusion microthermometry.

Author Contributions: Conceptualization, J.K. and K.Q.; methodology, J.K.; validation, J.K., K.Q. and L.W.; investigation, J.K., K.Q., K.H. and R.H.; resources, J.K.; writing—original draft preparation, J.K.; writing—review and editing, J.K. and L.W.; visualization, J.K.; supervision, K.Q. and L.W.; project administration, K.Q. All authors have read and agreed to the published version of the manuscript.

Funding: This research was funded by the National Natural Science Foundation of China, grant number 42202085, and the National Key Research and Development Program of China, grant number 2017YFC0601306.

Data Availability Statement: The data presented in this study are available in Supplementary Materials (Tables S1–S3).

Acknowledgments: We are grateful to Long Han, Qiang Zhao and the other local geologists of No.9 Geological Exploration Institute of Heilongjiang Province and Jinshi Mining Company Limited for assistance with the field work. The academic editor and two anonymous reviewers greatly helped to improve the manuscript.

Conflicts of Interest: The authors declare no conflict of interest.

References

1. Zeng, Q.D.; Liu, J.M.; Qin, K.Z.; Fan, H.R.; Chu, S.X.; Wang, Y.B.; Zhou, L.L. Types, characteristics, and time-space distribution of molybdenum deposits in China. *Int. Geol. Rev.* **2013**, *55*, 1311–1358. [CrossRef]
2. Qin, K.Z.; Zhai, M.G.; Li, G.M.; Zhao, J.X.; Zeng, Q.D.; Gao, J.; Xiao, W.J.; Li, J.L.; Sun, S. Links of collage orogenesis of multiblocks and crust evolution to characteristic metallogeneses in China. *Acta Petrol. Sin.* **2017**, *33*, 305–325. (In Chinese with English Abstract)
3. Zhao, C.; Qin, K.Z.; Song, G.X.; Li, G.M.; Li, Z.Z. Early Palaeozoic high-Mg basalt-andesite suite in the Duobaoshan Porphyry Cu deposit, NE China: Constraints on petrogenesis, mineralization, and tectonic setting. *Gondwana Res.* **2019**, *71*, 91–116. [CrossRef]
4. Zeng, Q.D.; Liu, J.M.; Chu, S.X.; Wang, Y.B.; Sun, Y.; Duan, X.X.; Zhou, L.L.; Qu, W.J. Re–Os and U–Pb geochronology of the Duobaoshan porphyry Cu–Mo–(Au) deposit, northeast China, and its geological significance. *J. Asian Earth Sci.* **2014**, *79*, 895–909. [CrossRef]
5. Hao, Y.J.; Ren, Y.S.; Duan, M.X.; Tong, K.Y.; Chen, C.; Yang, Q.; Li, C. Metallogenic events and tectonic setting of the Duobaoshan ore field in Heilongjiang Province, NE China. *J. Asian Earth Sci.* **2015**, *97*, 442–458. [CrossRef]
6. Li, N.; Sun, Y.L.; Li, J.; Li, W.B. Molybdenite Re/Os age of Wunugetu Shan porphyry Cu/Mo deposit, Inner Mongolia, and its implication for metallgenic geodynamics. *Acta Petrol. Sin.* **2007**, *23*, 2881–2888. (In Chinese with English Abstract)
7. Wang, Y.H.; Zhao, C.B.; Zhang, F.F.; Liu, J.J.; Wang, J.P.; Peng, R.M.; Liu, B. SIMS zircon U-Pb and molybdenite Re-Os geochronology, Hf isotope, and whole-rock geochemistry of the Wunugetushan porphyry Cu-Mo deposit and granitoids in NE China and their geological significance. *Gondwana Res.* **2015**, *28*, 1228–1245. [CrossRef]
8. Feng, Y.Z.; Chen, H.Y.; Xiao, B.; Li, R.C.; Deng, C.Z.; Han, J.S.; Li, G.H.; Shi, H.L.; Lai, C. Late Mesozoic magmatism at Xiaokelehe Cu-Mo deposit in Great Xing'an Range, NE China: Geodynamic and metallogenic implications. *Lithos* **2020**, *374–375*, 105713. [CrossRef]
9. Sun, Y.G.; Li, B.L.; Ding, Q.F.; Qu, Y.; Wang, C.K.; Wang, L.L.; Xu, Q.L. Mineralization Age and Hydrothermal Evolution of the Fukeshan Cu (Mo) Deposit in the Northern Great Xing'an Range, Northeast China: Evidence from Fluid Inclusions, H–O–S–Pb Isotopes, and Re–Os Geochronology. *Minerals* **2020**, *10*, 591. [CrossRef]
10. Wu, C.; Jiang, T.; Liu, W.; Zhang, D.; Zhou, Z. Early Cretaceous adakitic granites and mineralization of the Yili porphyry Mo deposit in the Great Xing'an Range: Implications for the geodynamic evolution of northeastern China. *Int. Geol. Rev.* **2015**, *57*, 1152–1171. [CrossRef]
11. Richards, J.P. The oxidation state, and sulfur and Cu contents of arc magmas: Implications for metallogeny. *Lithos* **2015**, *233*, 27–45. [CrossRef]
12. Richards, J.P. Porphyry copper deposit formation in arcs: What are the odds? *Geosphere* **2022**, *18*, 130–155. [CrossRef]
13. Richards, J.P.; Jourdan, F.; Creaser, R.A.; Maldonado, G.; DuFrane, S.A. Geology, geochemistry, geochronology, and economic potential of Neogene volcanic rocks in the Laguna Pedernal and Salar de Aguas Calientes segments of the Archibarca lineament, northwest Argentina. *J. Volcanol. Geotherm. Res.* **2013**, *258*, 47–73. [CrossRef]

14. Audetat, A. The Metal Content of Magmatic-Hydrothermal Fluids and Its Relationship to Mineralization Potential. *Econ. Geol.* **2019**, *114*, 1033–1056. [CrossRef]
15. Sun, W.D.; Arculus, R.J.; Kamenetsky, V.S.; Binns, R.A. Release of gold-bearing fluids in convergent margin magmas prompted by magnetite crystallization. *Nature* **2004**, *431*, 975–978. [CrossRef]
16. Zhou, T.C.; Zeng, Q.D.; Chu, S.X.; Zhou, L.L.; Yang, Y.H. Magmatic oxygen fugacities of porphyry Mo deposits in the East Xing'an-Mongolian Orogenic Belt (NE China) with metallogenic implications. *J. Asian Earth Sci.* **2018**, *165*, 145–159. [CrossRef]
17. Landtwing, M.R.; Pettke, T.; Halter, W.E.; Heinrich, C.A.; Redmond, P.B.; Einaudi, M.T.; Kunze, K. Copper deposition during quartz dissolution by cooling magmatic–hydrothermal fluids: The Bingham porphyry. *Earth Planet Sci. Lett.* **2005**, *235*, 229–243. [CrossRef]
18. Polya, D.A. Efficiency of hydrothermal ore formation and the Panasqueira W-Cu(Ag)-Sn vein deposit. *Nature* **1988**, *333*, 838–841. [CrossRef]
19. Zhang, D.H.; Jin, X.D.; Mao, S.D.; Wang, L.L. The classification of ore-forming fluid and the efficiency of ore formation of magmatic hydrothermal solution. *Earth Sci. Front.* **2011**, *18*, 90–102. (In Chinese with English Abstract)
20. Sanderson, D.J.; Roberts, S.; Gumiel, P.; Greenfield, C. Quantitative Analysis of Tin- and Tungsten-Bearing Sheeted Vein Systems. *Econ. Geol.* **2008**, *103*, 1043–1056. [CrossRef]
21. Heinrich, C. The physical and chemical evolution of low-salinity magmatic fluids at the porphyry to epithermal transition: A thermodynamic study. *Miner Depos.* **2005**, *39*, 864–889. [CrossRef]
22. Rusk, B.G.; Reed, M.H.; Dilles, J.H. Fluid Inclusion Evidence for Magmatic-Hydrothermal Fluid Evolution in the Porphyry Copper-Molybdenum Deposit at Butte, Montana. *Econ. Geol.* **2008**, *103*, 307–334. [CrossRef]
23. Hezarkhani, A.; Williams-Jones, A.E.; Gammons, C.H. Factors controlling copper solubility and chalcopyrite deposition in the Sungun porphyry copper deposit, Iran. *Miner. Depos.* **1999**, *34*, 770–783. [CrossRef]
24. Zhang, D.H.; Zhang, W.Z.; Xu, G.J. Exsolution and evolution of magmatic hydrothermal fluids and their constraints on the porphyry ore-forming system. *Earth Sci. Front.* **2001**, *8*, 193–202. (In Chinese with English Abstract)
25. Cline, J.S.; Bodnar, R.J. Can economic porphyry copper mineralization be generated by a typical calc-alkaline melt? *J. Geophys. Res. Solid Earth* **1991**, *96*, 8113–8126. [CrossRef]
26. Bodnar, R.J. Fluid-inclusion evidence for a magmatic source for metals in porphyry copper deposits. *Magma Fluid Ore Depos.* **1995**, *23*, 139–152.
27. Carroll, M.R.; Webster, J.D. Solubilities of sulfur, noble gases, nitrogen, chlorine, and fluorine in magmas. In *Volatiles in Magmas*; Walter de Gruyter GmbH: Berlin, Germany, 1994.
28. Candela, P.A. Controls on ore metal ratios in granite-related ore systems—An experimental and computational approach. *Trans. R. Soc. Edinb.-Earth Sci.* **1992**, *83*, 317–326.
29. Sibson, R.H. Roughness at the base of the seismogenic zone: Contributing factors. *J. Geophys. Res.* **1984**, *89*, 5791–5799. [CrossRef]
30. Koide, H.; Bhattacharji, S. Formation of fractures around magmatic intrusions and their role in ore localization. *Econ. Geol.* **1975**, *70*, 781–799. [CrossRef]
31. Mao, W.; Zhong, H.; Zhu, W.G.; Lin, X.G.; Zhao, X.Y. Magmatic-hydrothermal evolution of the Yuanzhuding porphyry Cu-Mo deposit, South China: Insights from mica and quartz geochemistry. *Ore Geol. Rev.* **2018**, *101*, 765–784. [CrossRef]
32. Audetat, A.; Pettke, T.; Heinrich, C.A.; Bodnar, R.J. The Composition of Magmatic-Hydrothermal Fluids in Barren and Mineralized Intrusions. *Econ. Geol.* **2008**, *103*, 877–908. [CrossRef]
33. Williams-Jones, A.E.; Heinrich, C.A. 100th Anniversary special paper: Vapor transport of metals and the formation of magmatic-hydrothermal ore deposits. *Econ. Geol.* **2005**, *100*, 1287–1312. [CrossRef]
34. Heinrich, C.A.; Gunthler, D. Metal fractionation between magmatic brine and vapor, determined by microanalysis of fluid. *Geology* **1999**, *27*, 755–758. [CrossRef]
35. Proffett, J.M. Geology of the Bajo de la Alumbrera Porphyry Copper-Gold Deposit, Argentina. *Econ. Geol.* **2003**, *98*, 1535–1574. [CrossRef]
36. Proffett, J.M. High Cu grades in porphyry Cu deposits and their relationship to emplacement depth of magmatic sources. *Geology* **2009**, *37*, 675–678. [CrossRef]
37. Chen, Y.J.; Wang, P.; Li, N.; Yang, Y.F.; Pirajno, F. The collision-type porphyry Mo deposits in Dabie Shan, China. *Ore Geol. Rev.* **2017**, *81*, 405–430. [CrossRef]
38. Audetat, A.; Edmonds, M. Magmatic-Hydrothermal Fluids. *Elements* **2020**, *16*, 401–406. [CrossRef]
39. Munoz, J.L. Calculation of HF and HCl fugacities from biotite compositions: Revised equations. *Geol. Soc. Am. Abstr. Program* **1992**, *24*, A221.
40. Abdel-Rahman, A.F.M. Nature of biotites from alkaline, calc-alkaline, and peraluminous magmas. *J. Petrol.* **1994**, *35*, 525–541. [CrossRef]
41. Wones, D.R.; Eugster, H.P. Stability of biotite—Experiment theory and application. *Am. Mineral* **1965**, *50*, 1228–1272.
42. Trail, D.; Watson, E.B.; Tailby, N.D. Ce and Eu anomalies in zircon as proxies for the oxidation state of magmas. *Geochim. Cosmochim. Acta* **2012**, *97*, 70–87. [CrossRef]
43. Loucks, R.R.; Fiorentini, M.L.; Henriquez, G.J. New Magmatic Oxybarometer Using Trace Elements in Zircon. *J. Petrol.* **2020**, *61*, egaa034. [CrossRef]

44. Liu, Y.J.; Feng, Z.Q.; Jiang, L.W.; Jin, W.; Li, W.M.; Guan, Q.B.; Wen, Q.B.; Liang, C.Y. Ophiolite in the eastern Central Asian Orogenic Belt, NE China. *Acta Petrol. Sin.* **2019**, *35*, 3017–3047. (In Chinese with English Abstract)
45. Wu, F.Y.; Zhao, G.C.; Sun, D.Y.; Wilde, S.A.; Yang, J.H. The Hulan Group: Its role in the evolution of the Central Asian Orogenic Belt of NE China. *J. Asian Earth Sci.* **2007**, *30*, 542–556. [CrossRef]
46. Li, Y.; Xu, W.L.; Tang, J.; Pei, F.P.; Wang, F.; Sun, C.Y. Geochronology and geochemistry of Mesozoic intrusive rocks in the Xing'an Massif of NE China: Implications for the evolution and spatial extent of the Mongol–Okhotsk tectonic regime. *Lithos* **2018**, *304*, 57–73. [CrossRef]
47. Goldstein, R.H.; Reynolds, T.J. *Systematics of Fluid Inclusions in Diagenetic Minerals*; SEPM Short Course: Broken Arrow, OK, USA, 1994.
48. Audetat, A.; Gunther, D. Mobility and H_2O loss from fluid inclusions in natural quartz crystals. *Contrib. Miner. Petrol.* **1999**, *137*, 1–14. [CrossRef]
49. Becker, S.P.; Fall, A.; Bodnar, R.J. Synthetic fluid inclusions. XVII. PVTX properties of high salinity H_2O-NaCl solutions (>30 wt% NaCl): Application to fluid inclusions that homogenize by halite disappearance from porphyry copper and other hydrothermal ore deposits. *Econ. Geol.* **2008**, *103*, 539–554. [CrossRef]
50. Thompson, J.M.; Meffre, S.; Danyushevsky, L. Impact of air, laser pulse width and fluence on U–Pb dating of zircons by LA-ICPMS. *J. Anal. At. Spectrom.* **2018**, *33*, 221–230. [CrossRef]
51. Paton, C.; Woodhead, J.D.; Hellstrom, J.C.; Hergt, J.M.; Maas, R. Improved laser ablation U-Pb zircon geochronology through robust downhole fractionation correction. *Geochem. Geophys. Geosyst.* **2010**, *11*, Q0AA06. [CrossRef]
52. Nachit, H.; Ibhi, A.; Abia, E.H.; Ben Ohoud, M. Discrimination between primary magmatic biotites, reequilibrated biotites and neoformed biotites. *CR Geosci.* **2005**, *337*, 1415–1420. [CrossRef]
53. Rasmussen, K.L.; Mortensen, J.K. Magmatic petrogenesis and the evolution of (F:Cl:OH) fluid composition in barren and tungsten skarn-associated plutons using apatite and biotite compositions: Case studies from the northern Canadian Cordillera. *Ore Geol. Rev.* **2013**, *50*, 118–142. [CrossRef]
54. Zhang, W.; Lentz, D.R.; Thorne, K.G.; McFarlane, C. Geochemical characteristics of biotite from felsic intrusive rocks around the Sisson Brook W-Mo-Cu deposit, west-central New Brunswick: An indicator of halogen and oxygen fugacity of magmatic systems. *Ore Geol. Rev.* **2016**, *77*, 82–96. [CrossRef]
55. Kumar, S.; Pathak, M. Mineralogy and geochemistry of biotites from Proterozoic granitoids of western Arunachal Himalaya: Evidence of bimodal granitogeny and tectonic affinity. *J. Geol. Soc. India* **2010**, *75*, 715–730. [CrossRef]
56. Stone, D. Temperature and pressure variations in suites of Archean felsic plutonic rocks, Berens River area, northwest Superior Province, Ontario, Canada. *Can. Miner.* **2000**, *38*, 455–470. [CrossRef]
57. Li, X.Y.; Zhang, C.; Behrens, H.; Holtz, F. Calculating biotite formula from electron microprobe analysis data using a machine learning method based on principal components regression. *Lithos* **2020**, *356–357*, 105371. [CrossRef]
58. Henry, D.J.; Guidotti, C.V.; Thomson, J.A. The Ti-saturation surface for low-to-medium pressure metapelitic biotites: Implications for geothermometry and Ti-substitution mechanisms. *Am. Miner.* **2005**, *90*, 316–328. [CrossRef]
59. Uchida, E.; Endo, S.; Makino, M. Relationship between solidification depth of granitic rocks and formation of hydrothermal ore deposits. *Resour. Geol.* **2007**, *57*, 47–56. [CrossRef]
60. Foster, M.D. Interpretation of the composition of trioctahedral micas. *US Geol. Surv. Prof. Paper B* **1960**, *354*, 11–49.
61. Boynton, W.V. Chapter 3—Cosmochemistry of the Rare Earth Elements: Meteorite Studies. In *Developments in Geochemistry*; Henderson, P., Ed.; Elsevier: Amsterdam, The Netherlands, 1984; Volume 2, pp. 63–114.
62. Li, W.K.; Cheng, Y.Q.; Yang, Z.M. Geo-fO_2: Integrated Software for Analysis of Magmatic Oxygen Fugacity. *Geochem. Geophys. Geosyst.* **2019**, *20*, 2542–2555.
63. Ferry, J.M.; Watson, E.B. New thermodynamic models and revised calibrations for the Ti-in-zircon and Zr-in-rutile thermometers. *Contrib. Miner. Petrol.* **2007**, *154*, 429–437. [CrossRef]
64. Fu, B.; Page, F.Z.; Cavosie, A.J.; Fournelle, J.; Kita, N.T.; Lackey, J.S.; Wilde, S.A.; Valley, J.W. Ti-in-zircon thermometry: Applications and limitations. *Contrib. Miner. Petrol.* **2008**, *156*, 197–215. [CrossRef]
65. Blundy, J.; Wood, B. Prediction of crystal-melt partition-coefficients from Elastic-Moduli. *Nature* **1994**, *372*, 452–454. [CrossRef]
66. Ballard, J.R.; Palin, J.M.; Campbell, I.H. Relative oxidation states of magmas inferred from Ce(IV)/Ce(III) in zircon: Application to porphyry copper deposits of northern Chile. *Contrib. Miner. Petrol.* **2002**, *144*, 347–364. [CrossRef]
67. Hoskin, P.W.O.; Black, L.P. Metamorphic zircon formation by solid-state recrystallization of protolith igneous zircon. *J. Metamorph. Geol.* **2000**, *18*, 423–439. [CrossRef]
68. Hoskin, P.W.O.; Schaltegger, U. The composition of zircon and igneous and metamorphic petrogenesis. *Rev. Mineral. Geochem.* **2003**, *53*, 27–62. [CrossRef]
69. Hall, D.L.; Sterner, S.M.; Bodnar, R.J. Freezing point depression of NaCl-KCl-H_2O solutions. *Econ. Geol.* **1988**, *83*, 197–202. [CrossRef]
70. Shao, J.L. *Prospecting Mineralogy of Gold Ore*; China University of Geosciences Press: Wuhan, China, 1988.
71. Watson, E.B.; Wark, D.A.; Thomas, J.B. Crystallization thermometers for zircon and rutile. *Contrib. Miner. Petrol.* **2006**, *151*, 413–433. [CrossRef]
72. Shen, P.; Hattori, K.; Pan, H.D.; Jackson, S.; Seitmuratova, E. Oxidation Condition and Metal Fertility of Granitic Magmas: Zircon Trace-Element Data from Porphyry Cu Deposits in the Central Asian Orogenic Belt. *Econ. Geol.* **2015**, *110*, 1861–1878. [CrossRef]

73. Strong, D.F. Ore deposit models—5—A model for granophile mineral-deposits. *Geosci. Can.* **1981**, *8*, 155–161.
74. Robb, L.J. *Introduction to Ore-Forming Processes*; Blackwell Publishing Company: Hoboken, NJ, USA, 2005.
75. Hu, R.G.; Zhao, Y.L.; Cai, Y.F.; Feng, Z.H.; Liu, X.J.; Zhou, Z.H.; Sha, P.Z. Characteristics of Biotite in the Granite Porphyry and Its Significance for Petrogenesis and Mineralization of Dachang Sn-Polymetallic Ore Deposit, Guangxi. *Earth Sci.* **2020**, *45*, 14. (In Chinese with English Abstract)
76. Zhang, S.H.; Li, W.X.; Zhou, X.X.; Yang, D.S.; Lv, P.L. Chemical composition of biotite from Wushan copper deposit, Jiangxi Province: Geology and metallogenic significances. *Geochimica* **2020**, *49*, 637–652. (In Chinese with English Abstract)
77. Trail, D.; Watson, E.B.; Tailby, N.D. The oxidation state of Hadean magmas and implications for early Earth's atmosphere. *Nature* **2011**, *480*, 79-U238. [CrossRef]
78. Zou, X.Y.; Qin, K.Z.; Han, X.L.; Li, G.M.; Evans, N.J.; Li, Z.Z.; Yang, W. Insight into zircon REE oxy-barometers: A lattice strain model perspective. *Earth Planet Sci. Lett.* **2019**, *506*, 87–96. [CrossRef]
79. Lu, Y.J.; Loucks, R.R.; Fiorentini, M.; Mccuaig, T.C.; Kobussen, A. *Zircon Compositions as a Pathfinder for Porphyry Cu ± Mo ± Au Deposits*; Society of Economic Geologists: Littleton, CO, USA, 2016; pp. 329–347.
80. Qiu, K.-F.; Marsh, E.; Yu, H.-C.; Pfaff, K.; Gulbransen, C.; Gou, Z.-Y.; Li, N. Fluid and metal sources of the Wenquan porphyry molybdenum deposit, Western Qinling, NW China. *Ore Geol. Rev.* **2017**, *86*, 459–473. [CrossRef]
81. Meng, X.Y.; Mao, J.W.; Zhang, C.Q.; Zhang, D.Y.; Liu, H. Melt recharge, f (O_2)-T conditions, and metal fertility of felsic magmas: Zircon trace element chemistry of Cu-Au porphyries in the Sanjiang orogenic belt, southwest China. *Min. Depos.* **2018**, *53*, 649–663. [CrossRef]
82. Sillitoe, R.H. Porphyry Copper Systems. *Econ. Geol.* **2010**, *105*, 3–41. [CrossRef]
83. Cloos, M. Bubbling magma chambers, cupolas, and porphyry copper deposits. *Int. Geol. Rev.* **2001**, *43*, 285–311. [CrossRef]
84. Seedorff, E.; Barton, M.D.; Stavast, W.J.A.; Maher, D.J. Root Zones of Porphyry Systems: Extending the Porphyry Model to Depth. *Econ. Geol.* **2008**, *103*, 939–956. [CrossRef]
85. Runyon, S.E.; Steele-Macinnis, M.; Seedorff, E.; Lecumberri-Sanchez, P.; Mazdab, F.K. Coarse muscovite veins and alteration deep in the Yerington batholith, Nevada: Insights into fluid exsolution in the roots of porphyry copper systems. *Min. Depos.* **2017**, *52*, 463–470. [CrossRef]
86. Qin, K.Z.; Zhao, J.X.; Fan, H.R.; Tang, D.M.; Li, G.M.; Yu, K.L.; Cao, M.J.; Su, B.X. On the ore-forming depth and possible maximum vertical extension of the major type ore deposits. *Earth Sci. Front.* **2021**, *28*, 271–294. (In Chinese with English Abstract)
87. Huang, M.-L.; Bi, X.-W.; Richards, J.P.; Hu, R.-Z.; Xu, L.-L.; Gao, J.-F.; Zhu, J.-J.; Zhang, X.-C. High water contents of magmas and extensive fluid exsolution during the formation of the Yulong porphyry Cu-Mo deposit, eastern Tibet. *J. Asian Earth Sci.* **2019**, *176*, 168–183. [CrossRef]
88. Burnham, C.W. Magmas and hydrothermal fluids. In *Geochemistry of Hydrothermal Ore Deposits*; Wiley: New York, NY, USA, 1979; pp. 71–136.
89. Whitney, J.A.; Naldrett, A.J. *Ore Deposition Associated with Magmas*; Open Library: El Paso, TX, USA, 1989.
90. Li, Z.-Z.; Qin, K.-Z.; Li, G.-M.; Jin, L.-Y.; Song, G.-X.; Han, R. Incursion of meteoric water triggers molybdenite precipitation in porphyry Mo deposits: A case study of the Chalukou giant Mo deposit. *Ore Geol. Rev.* **2019**, *109*, 144–162. [CrossRef]
91. Cline, J.S.; Bodnar, R.J. Direct Evolution of Brine from a Crystallizing Silicic Melt at the Questa, New-Mexico, Molybdenum Deposit. *Econ. Geol. Bull. Soc. Econ. Geol.* **1994**, *89*, 1780–1802. [CrossRef]
92. Henley, R.W.; Mcnabb, A. Magmatic vapor plume and ground-water interaction in porphyry copper emplacement. *Econ. Geol.* **1978**, *73*, 1–20. [CrossRef]
93. Redmond, P.B.; Einaudi, M.T.; Inan, E.E.; Landtwing, M.R.; Heinrich, C.A. Copper deposition by fluid cooling in intrusion-centered systems: New insights from the Bingham porphyry ore deposit, Utah. *Geology* **2004**, *32*, 217–220. [CrossRef]
94. Sourirajan, S.; Kennedy, G.C. System H_2O-NaCl at elevated temperatures and pressures. *Am. J. Sci.* **1962**, *260*, 115. [CrossRef]
95. Haas, J.L. Physical properties of the coexisting phases and thermochemical properties of the H_2O component in boiling NaCl solutions. *US Geol. Surv. Bull.* **1976**, *1421*, 1–73.
96. Fournier, R.O. Hydrothermal processes related to movement of fluid from plastic into brittle rock in the magmatic-epithermal environment. *Econ. Geol.* **1999**, *94*, 1193–1211. [CrossRef]
97. Hang, S.; Zhang, L.; Li, K.; Chen, Z.; Wu, H.; Xiang, P.; Zhang, X. CH_4-containing fluid inclusion study of the Taipingchuan porphyry Cu-Mo deposit, Inner Mongolia. *Acta Petrol. Sin.* **2010**, *26*, 1386–1396.
98. Li, N.; Chen, Y.J.; Lai, Y.; Li, W.B. Fluid inclusion study of the Wunugetushan porphyry Cu-Mo deposit, Inner Mongolia. *Acta Petrol. Sin.* **2007**, *23*, 2177–2188. (In Chinese with English Abstract)
99. Shi, Q.; Lai, Y.; Guo, H.; Kang, Y.; Liu, C. Fluid inclusion and C-O isotopic constrains on the origin and evolution of ore-forming fluids of the Badaguan Cu-Mo deposit, Inner Mongolia. *Ore Geol. Rev.* **2021**, *136*, 104267. [CrossRef]
100. Candela, P.A.; Holland, H.D. The partitioning of copper and molybdenum between silicate melts and aqueous fluids. *Geochim Cosmochim. Acta* **1984**, *48*, 373–380. [CrossRef]
101. Keppler, H.; Wyllie, P.J. Partitioning of Cu, Sn, Mo, W, U, and Th between melt and aqueous fluid in the systems haplogranite-H_2O HCl and haplogranite-H_2O HF. *Contrib. Miner. Petrol.* **1991**, *109*, 139–150. [CrossRef]
102. Candela, P.A. Calculation of magmatic fluid contributions to porphyry-type ore systems—Predicting fluid inclusion chemistries. *Geochem. J.* **1989**, *23*, 295–305. [CrossRef]

103. Webster, J.D.; Vivo, B.D. Experimental and modeled solubilities of chlorine in aluminosilicate melts, consequences of magma evolution, and implications for exsolution of hydrous chloride melt at Mt. Somma-Vesuvius. *Am. Miner.* **2002**, *87*, 1046–1061. [CrossRef]
104. Zajacz, Z.; Halter, W.E.; Pettke, T.; Guillong, M. Determination of fluid/melt partition coefficients by LA-ICPMS analysis of co-existing fluid and silicate melt inclusions: Controls on element partitioning. *Geochim. Cosmochim. Acta* **2008**, *72*, 2169–2197. [CrossRef]
105. Chevychelov, V. Partitioning of Pb, Zn, W, Mo, Cl, and major elements between aqueous fluid and melt in the systems granodiorite (granite, leucogranite)-H_2O-NaCl-HCl V. Yu. Chevychelov and T. K. Chevychelova. *Neues Jahrb. Mineral. Abhandlungen.* **1997**, *172*, 101–115. [CrossRef]
106. Bai, T.B.; Koster van Groos, A.F. The distribution of Na, K, Rb, Sr, Al, Ge, Cu, W, Mo, La, and Ce between granitic melts and coexisting aqueous fluids. *Geochim. Cosmochim. Acta* **1999**, *63*, 1117–1131. [CrossRef]